ARL-TR-10429 ● SEP 2026

Mechanical Phase Identification at an SiC/Ti-6Al-4V Active-Braze Interface by k-Medoids Clustering of Nanoindentation Arrays

by Brady G. Butler, Efraín Hernández-Rivera, S. Gary Hirsch, Daniel O. Lewis, Trevor R. Hastings, and Michael T. Hurst

NOTICES

Disclaimers

The findings in this report are not to be construed as an official Department of the Army position unless so designated by other authorized documents.

Citation of manufacturer's or trade names does not constitute an official endorsement or approval of the use thereof.

Destroy this report when it is no longer needed. Do not return it to the originator.

This research was supported in part by ARL under Cooperative Agreements W911NF-22-2-0106 and W911-NF-22-F-0032.

During the preparation of this work, the authors utilized OpenAI's ChatGPT to assist in developing Python scripts for data processing and figure generation. All substantive analyses, interpretations, and conclusions remain solely the authors' own, and the authors assume full responsibility for the manuscript's integrity.

ARL-TR-10429 ● SEP 2026

Mechanical Phase Identification at an SiC/Ti-6Al-4V Active-Braze Interface by k-Medoids Clustering of Nanoindentation Arrays

Brady G. Butler, Efraín Hernández-Rivera, and S. Gary Hirsch
DEVCOM Army Research Laboratory

Daniel O. Lewis and Trevor R. Hastings
Texas A&M University

Michael T. Hurst
Bush Combat Development Complex

REPORT DOCUMENTATION PAGE

1. REPORT DATE	2. REPORT TYPE	3. DATES COVERED	
		START DATE	END DATE
September 2026	Technical Report	01 October 2022	30 September 2025

4. TITLE AND SUBTITLE
Mechanical Phase Identification at an SiC/Ti-6Al-4V Active-Braze Interface by k-Medoids Clustering of Nanoindentation Arrays

5a. CONTRACT NUMBER	5b. GRANT NUMBER	5c. PROGRAM ELEMENT NUMBER
W911NF-22-2-0106		
5d. PROJECT NUMBER	**5e. TASK NUMBER**	**5f. WORK UNIT NUMBER**

6. AUTHOR(S)
Brady G. Butler, Efraín Hernández-Rivera, S. Gary Hirsch, Daniel O. Lewis, Trevor R. Hastings, and Michael T. Hurst

7. PERFORMING ORGANIZATION NAME(S) AND ADDRESS(ES)	8. PERFORMING ORGANIZATION REPORT NUMBER
DEVCOM Army Research Laboratory ATTN: FCDD-RLA-MF Aberdeen Proving Ground, MD 21005	ARL-TR-10429

9. SPONSORING/MONITORING AGENCY NAME(S) AND ADDRESS(ES)	10. SPONSOR/MONITOR'S ACRONYM(S)	11. SPONSOR/MONITOR'S REPORT NUMBER(S)

12. DISTRIBUTION/AVAILABILITY STATEMENT
DISTRIBUTION STATEMENT A. Approved for public release: distribution unlimited.

13. SUPPLEMENTARY NOTES
ORCIDs: Brady G. Butler, 0000-0002-7677-9685; Efraín Hernández-Rivera, 0000-0002-7855-1027; Daniel O. Lewis, 0000-0002-3427-7265; Trevor R. Hastings, 0000-0003-4614-7019; Michael T. Hurst, 0000-0002-6138-2634

14. ABSTRACT
Spatially resolving mechanical properties across dissimilar-material interfaces remains challenging because microstructural features can approach the characteristic sampling volume of local mechanical measurements. Here, high-density nanoindentation was combined with microstructural characterization and spatial registration to examine a SiC/Ti-6Al-4V joint produced using an Ag-Cu-In-Ti active braze. Reference indentation measurements established the mechanical response of the SiC and Ti-6Al-4V end members, while 10- and 20-mN NanoBlitz arrays mapped mechanical variations across the interface. K-medoids clustering of hardness, modulus, and surface-height data was used to identify mechanically similar populations without incorporating lateral position; k-means provided an independent comparison. The mechanical maps reproduced the coarse architecture of the joint and identified distinct responses within the approximately 100-µm braze interlayer. However, narrow reaction layers, submicrometer constituents, and pore-affected measurements could not be interpreted as independent phases reliably. K-medoids provided experimentally traceable cluster representatives and reduced sensitivity to extreme measurements, although both algorithms produced similar results for well-separated populations. These results demonstrate that spatial resolution, sampling density, and correlative characterization ultimately govern mechanically based phase identification more strongly than the choice of clustering algorithm.

15. SUBJECT TERMS
nanoindentation, k-medoids clustering, mechanical phase identification, dissimilar-material interfaces, active brazing, Sciences of Extreme Materials

16. SECURITY CLASSIFICATION OF:			17. LIMITATION OF ABSTRACT	18. NUMBER OF PAGES
a. REPORT	b. ABSTRACT	C. THIS PAGE		
UNCLASSIFIED	UNCLASSIFIED	UNCLASSIFIED	UU	55

19a. NAME OF RESPONSIBLE PERSON	19b. PHONE NUMBER *(Include area code)*
Brady G. Butler	(520) 691-5844

STANDARD FORM 298 (REV. 5/2020)
Prescribed by ANSI Std. Z39.18

Contents

List of Figures

List of Tables

Acknowledgments

We wish to thank George Pharr, Jacob Hempel, and Christopher Walker of Texas A&M University for equipment and discussions that were critical to the success of this effort.

1. Introduction

Dissimilar metal/ceramic joints often derive their performance from an interfacial region that is small in dimension but complex in structure. Active brazing is a useful example. Reactive additions such as Ti promote bonding to ceramics, but the same reactions that enable wetting also produce chemically and mechanically distinct reaction products within the braze and adjacent substrates.[1–3] Consequently, the joint cannot necessarily be represented as two bulk materials separated by a homogeneous interlayer. Its local response depends on the phases that form, their spatial arrangement, and the mechanical contrast between neighboring constituents.

This distinction is particularly important when microstructural information is incorporated directly into mechanical models. In the SiC/Ti-6Al-4V joint considered here, spatially resolved compositional data can be converted into phase-informed finite-element meshes.[4] Such models require mechanical properties at approximately the same length scale as the features represented in the mesh. Bulk measurements of the ceramic, braze alloy, or Ti-6Al-4V substrate do not provide these values. Moreover, assigning properties solely from chemical composition is problematic because composition does not uniquely determine mechanical response, particularly within reaction layers containing solid solutions, intermetallic compounds, and composition gradients. Local mechanical measurements are therefore needed to complement chemical and microstructural characterization.

Instrumented indentation provides a practical means of probing mechanical response at this scale. Grid-indentation methods were developed to extract statistically meaningful mechanical information from heterogeneous microstructures by acquiring large numbers of spatially distributed measurements.[5,6] More recent high-speed nanoindentation techniques extend this concept by acquiring hundreds or thousands of measurements over experimentally useful areas, producing spatial maps of hardness, modulus, contact depth, and related quantities.[7] These methods have enabled mechanical mapping of multiphase alloys and other heterogeneous materials at length scales that are difficult to access using conventional mechanical tests.[8,9] This approach represents a shift from conventional workflows, in which phases are first identified and segmented before targeted mechanical measurements are performed. By acquiring dense indentation arrays without requiring prior phase identification, high-speed mapping reduces operator-dependent site selection and enables subsequent data-driven identification of mechanically distinct populations.

The interpretation of such maps, however, is not straightforward. An indentation measurement represents the response of a finite interaction volume rather than a point measurement of a single phase. Measurements near phase boundaries can therefore contain contributions from multiple constituents. Indentation depth and spacing further influence the extent to which individual phases can be distinguished, particularly when characteristic feature dimensions approach the indentation interaction volume.[8] Surface preparation, pile-up, porosity, and overlapping property distributions introduce additional variability. Consequently, mechanically distinct populations may not correspond one-to-one with phases identified by microscopy or compositional analysis. This limitation is fundamental to the interpretation of indentation-derived mechanical phase maps, rather than simply a problem of selecting the correct statistical algorithm.

Statistical deconvolution and clustering provide complementary approaches for extracting structure from these datasets. Distribution-based approaches have been used extensively to estimate the number and properties of mechanically distinct populations within indentation datasets, while Gaussian-mixture and related methods have expanded these analyses to multivariate property spaces.[10,11] Their performance depends on the degree of separation between constituent distributions and on assumptions concerning the underlying population shapes. Recent work has therefore emphasized both the selection of an appropriate analysis method and the importance of comparing indentation-derived populations with independently measured microstructural information.[8,9,12]

Partitional clustering provides another approach because it does not require the measured populations to follow prescribed probability distributions. K-means partitions observations around calculated cluster centroids and remains one of the most widely used methods for unsupervised classification.[13,14] K-medoids instead represents each cluster using an observed member of the dataset rather than a calculated centroid.[15] This distinction is attractive for nanoindentation because a medoid corresponds to an actual measurement with a defined spatial position and experimentally measured properties. Importantly, k-medoids analysis of grid-nanoindentation data is not new. Chen et al.[16] demonstrated its use for identifying mechanically distinct populations in cementitious materials and compared its performance with conventional statistical approaches. The more relevant question for complex interfaces is whether these mechanically derived clusters correspond to independently identified microstructural regions when both measurements are spatially registered.

The present work addresses this question using a SiC/Ti-6Al-4V joint produced with an Ag-Cu-In-Ti active braze. The interface provides a demanding test case because it contains the two dissimilar end members together with an Ag-rich braze

matrix and multiple reaction regions formed during joining. Microstructural and chemical characterization are first used to establish the constituent regions of the interface. Spatially registered optical segmentation is then used as an image-derived comparison for high-density NanoBlitz indentation arrays acquired across the same interfacial region. K-means and k-medoids clustering are applied to the indentation measurements to determine whether mechanically distinct populations can be identified without using spatial or compositional labels during clustering.

The objective is therefore not to demonstrate that a clustering algorithm can reproduce a predefined phase map. Rather, this study examines the conditions under which mechanically derived clusters correspond to independently characterized microstructural regions, where that correspondence breaks down, and how the result depends on the mechanical contrast and spatial scale of the interface. Bulk and local indentation measurements of the SiC and Ti-6Al-4V end members provide reference behavior for interpreting the interfacial arrays. This framework allows k-means and k-medoids to be evaluated as tools for spatially resolved mechanical phase identification while retaining the distinction between a chemical phase, an image-segmented region, and a mechanically measured population.

2. Methods

2.1 Sample Fabrication and Joining

The joint couples an approximately 6.35-mm-thick silicon carbide (α-SiC, Saint-Gobain Hexoloy SA) to an equally thick grade 5 titanium (i.e., Ti-6Al-4V, Ti64) substrate (ATI Specialty Materials) through an approximately 101.6-μm-thick InCuSil ABA active braze foil. InCuSil ABA is a low-melting-point silver–copper–indium alloy carrying 1.25 wt% titanium as the active constituent; the titanium reduces the interfacial energy against the ceramic and enables wetting without prior metallization. Alloy composition and the vendor-reported thermophysical and mechanical properties are given in Table 1.[17]

Table 1. InCuSil ABA active brazing alloy composition and vendor-reported properties.[17]

Property	InCuSil ABA
Composition (wt%)	59.0 Ag, 27.25 Cu, 12.5 In, 1.25 Ti
Melting range	715 °C liquidus/605 °C solidus
CTE (20–400 °C)	18.2×10^{-6} °C^{-1}
Thermal conductivity (calculated)	70 W m^{-1} K^{-1}
Density	9.7 g cm^{-3}
Yield strength (0.2% offset)	338 MPa
Tensile strength	455 MPa
Elongation (50-mm gauge)	21%
Recommended brazing temperature	715–740 °C
Recommended atmosphere	Vacuum (10^{-5} mm Hg) or inert gas

Note: CTE = coefficient of thermal expansion

Samples were brazed at 725 °C for 30 min, within the vendor-recommended window, with heating rates of approximately 5 °C min^{-1} under a vacuum better than 10^{-5} mm Hg.[4] The 30-min hold above the liquidus, combined with the slow ramp, provides ample time for the interdiffusion and is consistent with the roughly 100-µm interlayer and deep Ti and V penetration observed there.

Two features of Table 1 are consequential for what follows. First, the substantial CTE mismatch among SiC, Ti-6Al-4V, and the Ag-based braze is expected to generate residual stresses during cooling. Their local magnitude and sign depend on joint geometry, constituent properties, and plastic relaxation within the braze; therefore, no specific residual-stress state is assigned here without direct measurement or thermomechanical modeling.[18] Second, the 110 °C spread between solidus and liquidus permits substantial compositional partitioning during solidification, which is the origin of the multiphase structure documented below.

Cross sections were prepared by standard metallographic sectioning and mounting, ground with 320- and 600-grit SiC paper, polished with 9- and 3-µm diamond slurry, and finished with 0.05-µm colloidal silica for approximately 10 min. Surface finish sets the noise floor on the NanoBlitz depth channel; the extended colloidal-silica step also produces the differential polishing relief between hard and soft phases that makes surface height an informative clustering feature.

2.2 Microscopy and Phase Identification

Microscopy of the bonded region comprised secondary-electron and backscattered-electron (BSE) imaging together with X-ray energy dispersive spectroscopy (XEDS) mapping. Imaging used a Thermo Fisher Apreo S scanning electron microscope (SEM) and a Thermo Fisher Helios G4 DualBeam instrument; XEDS was collected with an EDAX Elite Super system and quantified in the APEX

software using standardless quantification. X-ray photoelectron spectroscopy (XPS) was performed on the braze zone with an aperture of approximately 100 μm.

Three detector configurations were used, which makes a significant difference when reading the micrographs. The Everhart–Thornley detector gives topographic secondary-electron contrast; an in-lens backscattered detector gives a first atomic-number contrast; and a dedicated concentric backscatter (CBS) detector, consisting of four concentric rings designated A (innermost) through D (outermost), gives markedly stronger compositional contrast. Summing all four rings improves overall contrast relative to either of the first two detectors, while using only the A ring weights the signal toward high-angle BSEs and therefore toward atomic number, at the cost of saturating in the highest-Z regions.

Because the XEDS measurements were obtained using standardless quantification, the reported compositions are treated primarily as comparative phase fingerprints rather than high-accuracy absolute chemical analyses.[19] Compositions should be read as phase fingerprints suitable for discriminating one reaction product from another, not as certified analyses. Elements present below approximately 2 at% are not reported. Carbon in particular cannot be reliably resolved by XEDS in this system, so the presence of interfacial carbides is inferred from morphology and from the reactivity of the active braze rather than measured directly.

2.3 Thermodynamic Assessment

A pseudo-binary section was computed between the InCuSil ABA composition and Ti-6Al-4V to establish which phases are thermodynamically accessible as the local composition traverses the interlayer. The section was computed in Thermo-Calc using the TCHEA v5.1 high-entropy-alloy database. The section is used qualitatively, to constrain the list of candidate phases; it is not used to predict phase fractions because it is unlikely that this interface reaches equilibrium during a braze cycle of this duration.

2.4 Supervised Optical Image Segmentation

Optical micrographs of the polished cross section were segmented using the Trainable WEKA Segmentation plugin in ImageJ.[20] The purpose of this segmentation was to generate a spatially continuous microstructural reference map that could be registered with the nanoindentation arrays. The segmentation was not used to establish phase chemistry or as an input to the mechanical clustering analysis.

Representative pixels within a manually labeled training region were assigned to five classes corresponding to the microstructural model established independently: SiC ceramic, Ti-6Al-4V substrate, Cu-Ti intermetallic, Cu-Ti-In face-centered cubic (FCC) alloy, and Ag-In-Cu FCC alloy. The classifier was trained using this labeled region and subsequently applied to a spatially separate analysis region containing the indentation arrays. Thus, the classification of the indentation region was based on optical appearance rather than prior knowledge of the indentation response.

Trainable WEKA Segmentation was operated using its standard multiscale image features and a FastRandomForest classifier. The configuration used for the reported segmentation is summarized in Table 2. The enabled features incorporate intensity, edge, and line- or boundary-sensitive information across multiple length scales. These features were sufficient to distinguish the major optical contrasts of the SiC, Ti-6Al-4V, braze matrix, and elongated reaction regions without introducing a microstructure-specific classifier architecture.

Table 2. Trainable WEKA Segmentation configuration.

Setting	Value
Plugin	Trainable WEKA Segmentation v4.0.0
Enabled features	Gaussian blur, Sobel filter, Hessian, difference of Gaussians, membrane projections
Minimum sigma	1.0
Maximum sigma	16.0
Membrane thickness	1 px
Membrane patch size	19 px
Classifier	FastRandomForest
Trees (-I)	200
Features per split (-K)	2
Random seed (-S)	1557655077

Following spatial registration, each indentation coordinate could therefore be associated with the optical class present at the center of the indent. This provides a simple experimental comparison between the local microstructure and the mechanically derived grouping. Similar registration of nanoindentation measurements with independently acquired microstructural maps has been demonstrated as a useful approach for examining local structure-property relationships.[12]

The optical classification at an indent center identifies the constituent exposed at the surface, but the measured indentation response reflects deformation within a finite subsurface volume and may therefore include contributions from neighboring constituents. This distinction is particularly important near phase boundaries and within narrow reaction layers, where the indentation interaction volume may

encompass more than one constituent. Likewise, optical contrast alone does not establish chemical or crystallographic phase identity. Phase assignments were therefore based on the complementary microstructural and compositional characterization; where these measurements and the optical segmentation differed, the independent characterization governed the interpretation.

The WEKA map is consequently used as an image-derived spatial reference rather than quantitative phase ground truth. No per-class accuracy metrics were calculated for the segmented analysis region, so the segmentation is not used independently to establish phase fractions or classifier accuracy. Its purpose is narrower: to provide a consistent, spatially resolved estimate of the microstructural region beneath each indent and thereby permit direct comparison with the independently derived mechanical maps.

2.5 Nanoindentation

All indentation was performed on a KLA iMicro with a Berkovich tip. A Poisson ratio of 0.2 was assumed for SiC and 0.35 for Ti64 in the reduced-modulus conversion. Hardness and modulus were extracted by the Oliver–Pharr method from the unloading compliance.[21] Three distinct test campaigns were run, illustrated schematically in Figure 1.

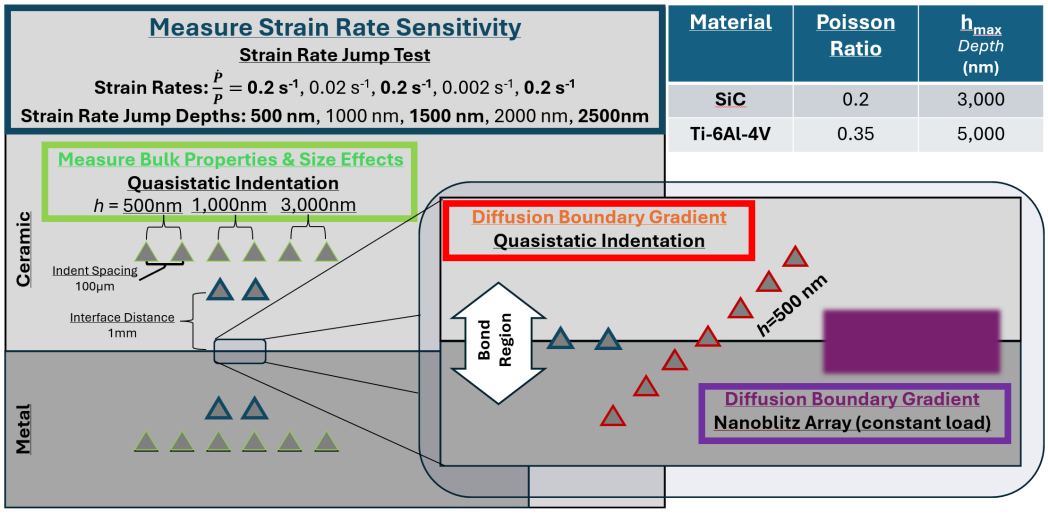

Figure 1. Indentation testing strategy for the bonded couple: quasi-static indents in the monolithic regions for bulk properties and size effects, strain-rate jump tests, and constant-load NanoBlitz arrays across the diffusion boundary.

2.5.1 Bulk Reference Properties

Quasi-static indents were placed in monolithic SiC and monolithic Ti64 at least 1 mm from the interface, with 100 µm spacing, to depths of 500, 1000, and

3000 nm. Maximum depths of 3000 nm (SiC) and 5000 nm (Ti64) were used for the deepest tests. Ten tests were run in each material.

2.5.2 Indentation Size Effect

Instrumented indentation commonly shows a depth dependence of hardness, with higher apparent hardness at shallow depth. The effect is attributed to strain gradients and local lattice curvature, which require additional geometrically necessary dislocations to accommodate the deformation imposed by the indenter.[22] Large indents suppress the effect and give hardness values representative of the bulk, but it is more informative to fit the asymptotic decay directly using the Nix–Gao relation:[23]

$$H^2(h) = H_0^2\left(1 + \frac{h^*}{h}\right), \tag{1}$$

where H is hardness at contact depth h, H_0 is the asymptotic hardness at infinite depth, and h^* is a characteristic length reflecting the strength and spatial extent of gradient-driven hardening. In practice, H^2 is plotted against $1/h$ and fitted over a depth window that excludes very shallow data affected by tip rounding and surface artifacts; the intercept gives H_0^2 and the slope gives $H_0^2 h^*$. H_0 is therefore the size-effect-free bulk hardness and h^* the characteristic length scale of strain-gradient plasticity hardening.

Shallow-depth cutoffs of 0.29 μm (Ti64) and 0.30 μm (SiC) were applied before fitting. Residuals against fitted H^2 are reported alongside the fits, because a Nix–Gao fit that is visually acceptable can still carry strong systematic structure in its residuals.

2.5.3 Strain-Rate Sensitivity (SRS)

SRS was determined following the strain-rate jump approach of Maier et al.,[24] in which hardness is measured at several constant indentation strain rates within a single indentation cycle by imposing step changes in the loading rate while monitoring displacement continuously. Formally, the SRS exponent, m, is defined as

$$m = \frac{\partial \ln(H)}{\partial \ln(\dot{\varepsilon})}, \tag{2}$$

where the equivalent indentation strain rate is approximated as $\dot{\varepsilon} \approx (1/h)(\partial h/\partial t)$. Because the controlling variable in load-controlled nanoindentation is the load P or loading rate $\dot{P}$, the applied strain rate is approximated for self-similar geometries as $\dot{\varepsilon} \approx (1/2)(\dot{P}/P)$.

Hardness in indentation is itself depth dependent, so a direct comparison of hardness measured at different depths would fold the indentation size effect into the apparent rate sensitivity. To isolate the rate contribution, hardness–depth trends within each constant-rate segment are linearly extrapolated to a common reference depth (at which the jump occurs) before the ratio is taken[24]:

$$m(h_{12}) = \frac{\ln\left(\frac{H_2(h_{12})}{H_1(h_{12})}\right)}{\ln\left(\frac{\dot{\varepsilon}_2}{\dot{\varepsilon}_1}\right)}. \quad (3)$$

The imposed rate sequence was $(\dot{P}/P)$ = 0.2, 0.02, 0.2, 0.002, 0.2 s^{-1}, with jumps at 500, 1000, 1500, 2000, and 2500 nm.

2.5.4 NanoBlitz Arrays Across the Interface

Two high-density constant-load arrays were placed across the braze zone: one at 10-mN peak load and one at 20 mN. Each array nominally comprises 400 indents at 10-µm pitch in both directions (40 columns along the joint by 10 rows across it) spanning approximately 400 µm parallel to the interface and 90 µm through the interlayer thickness, oriented so that rows run parallel to the joint. Each 400-indent array was screened independently before clustering using permissive, array-wide outlier criteria. Indents with hardness outside ±3 standard deviations of the array mean were removed first; the statistics were then recalculated, and indents with modulus outside ±3 standard deviations of the updated mean were removed. Records containing missing values were also excluded. This procedure retained 363 indents in the 10-mN array and 376 in the 20-mN array. Because the array-wide variance was dominated by the mechanical contrast between SiC and the metallic constituents, these bounds removed only extreme measurements and preserved the distinct mechanical populations. The removed measurements were not uniformly distributed but were concentrated primarily around pores and other defects. However, some anomalously low-hardness measurements associated with indents located in or near pores remained and were interpreted as an artifact population.

The two loads are complementary rather than redundant. The 10-mN array produces shallower indents and therefore samples a smaller volume, improving spatial resolution against the finer reaction products but increasing the influence of the indentation size effect and of surface roughness. The 20-mN array averages over a larger volume, giving lower scatter at the cost of more boundary mixing.

The same region of interest (ROI) was imaged optically before and after indentation (Figure 2), which allows each indent coordinate to be registered against the pristine microstructure rather than against a surface already modified by testing.

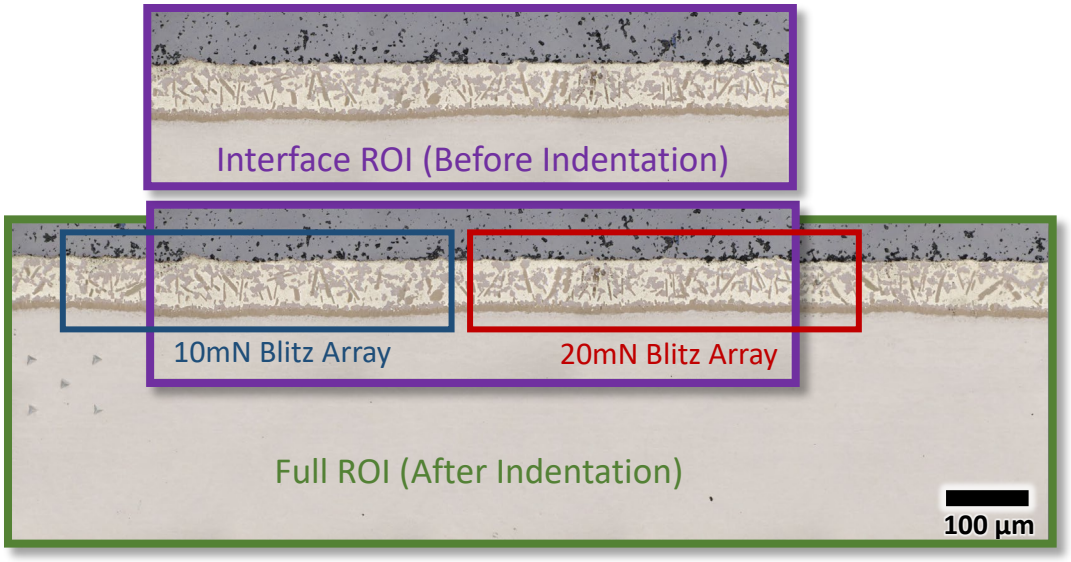

Figure 2. Optical images of ROIs before and after indentation, showing the pristine microstructure and the non-overlapping footprints of the 10- and 20-mN NanoBlitz arrays within the indented field.

2.6 Data-driven Phase Grouping

Each accepted indent provided hardness (H), reduced modulus (E), contact stiffness (S), penetration depth, and relative surface height (Z), together with derived quantities including Vickers hardness, ln(H), and ln(E).[21,25] Clustering was performed using a deliberately compact feature set comprising standardized ln(H), ln(E), and Z. Each feature was standardized prior to clustering to prevent differences in numerical scale from controlling the calculated distances. The lateral coordinates X and Y were excluded. Thus, the clustering algorithms were not provided with spatial position; spatial organization in the resulting cluster maps emerged from systematic variations in the measured indentation and surface-response variables.

The feature set was selected to retain complementary physical information while limiting redundancy. Logarithmic transformation of H and E reduced the influence of the large property contrast between the SiC, braze, and Ti-6Al-4V regions and improved resolution of differences within the interfacial region. The Z coordinate provided a complementary measure of local surface relief. Following extended colloidal-silica polishing, mechanically dissimilar constituents can develop measurable topographic contrast; Z was therefore treated as an auxiliary surface-response variable rather than as a direct measurement of phase identity. The correlations among the candidate variables were also examined. Alternative feature sets, including (H, E), [ln(H), ln(E)], (H, E, S), and the full set of available numerical variables, were also evaluated as sensitivity tests. The compact [ln(H),

ln(E), Z] representation was carried forward because it retained the principal variations of the indentation maps without introducing strongly redundant variables.

Two partitional clustering approaches were applied independently to the same standardized data: k-means, using k-means++ initialization, and k-medoids using a partitioning-around-medoids formulation. K-means represents each cluster by a calculated centroid and minimizes squared distances between observations and their assigned centroids.[13,14] K-medoids instead represents each cluster by an observed member of the dataset and minimizes the summed dissimilarity between observations and their assigned medoids.[15,16] K-medoids was used as the primary analysis, while k-means provided a conventional benchmark for determining whether the principal interpretations depended on the choice of partitioning method.

The preference for k-medoids was motivated primarily by its experimental interpretability and reduced sensitivity to isolated extreme observations. High-density indentation maps of heterogeneous materials inevitably contain measurements influenced by constituent boundaries, small features, pores, surface relief, or interaction volumes that span more than one constituent.[5,6,8,12,26] Even after quality-control rejection of apparent outliers, some of these responses are physically meaningful and should not necessarily be removed as statistical outliers. Because the k-means objective weights large deviations quadratically, such observations can exert substantial influence on a calculated centroid.[13,14] The corresponding influence is reduced in a medoid-based partition because the representative is restricted to an observed measurement and the point-to-medoid dissimilarities are not squared.[15]

The use of observed representatives also provides a practical experimental advantage. Each medoid corresponds to a specific indent with measured properties, a load-displacement record, and a known location on the specimen. The representative of a mechanically identified group can therefore be traced directly back to the experiment and examined in the corresponding micrograph. This feature is particularly useful for spatially resolved indentation, and k-medoids has previously been applied successfully to the analysis of grid-nanoindentation datasets.[16] Importantly, this robustness does not make mixed or boundary indents equivalent to measurements of a discrete phase. An indent whose interaction volume spans multiple constituents remains a mixed mechanical measurement regardless of the clustering algorithm employed.[5,8] For this reason, the resulting groups are treated here as mechanically similar populations and are identified with specific microstructural regions only after comparison with independent microscopy.

The sensitivity to cluster number was examined over k = 2 to 10. The number of clusters was assessed from the elbow in within-cluster dispersion and from average silhouette width, which compares within-cluster cohesion with separation from the nearest neighboring cluster.[27] These measures were used as internal diagnostics rather than as independent evidence for the number of physical phases. For direct comparison with the microscopy-derived segmentation, the selected values of k were informed by the independently characterized microstructure. The resulting analysis therefore tests whether mechanically defined populations reproduce the expected microstructural partition at a comparable level of description; it is not intended as a fully unconstrained determination of the number of phases present.

2.7 Spatial Registration

Optical micrographs of the ROI were acquired before and after indentation and spatially registered using rigid translation and rotation. The registered images allowed the coordinates of each accepted indent to be transferred to the corresponding location in the pristine microstructure and the image segmentation. Indent centers identified in the post-indentation image were therefore associated with the corresponding image-derived class in the registered pre-indentation field. Sensitivity to pixel-scale segmentation variability was examined using local sampling or smoothing radii of 3, 5, and 10 pixels.

The registration was used for comparison, not for clustering. Neither the image-segmentation labels nor the lateral coordinates X and Y were supplied to k-means or k-medoids. Consequently, correspondence between a mechanical cluster and a microstructural region represents agreement between independently derived descriptions of the same area rather than supervised classification. This distinction follows the correlative mapping approach used in spatially resolved nanoindentation studies, where mechanical measurements are registered against independently acquired microstructural or compositional information.[9,12] The image segmentation is therefore treated as a registered microstructural baseline rather than as absolute phase ground truth.

3. Results and Discussion

3.1 Interface Morphology

Secondary-electron and BSE micrographs of the bonded region (Figure 3) establish the basic architecture of the joint. The SiC occupies the top of the field and appears dark; it contains abundant porosity and is clearly not fully dense, which becomes important when the indentation arrays are interpreted. The bottom of the field is Ti-

6Al-4V showing its characteristic α/β structure. Between them lies an Ag-rich braze zone approximately 100 µm thick. Three major phases are evident within that zone, and at least two further phases appear along the boundary with the Ti64.

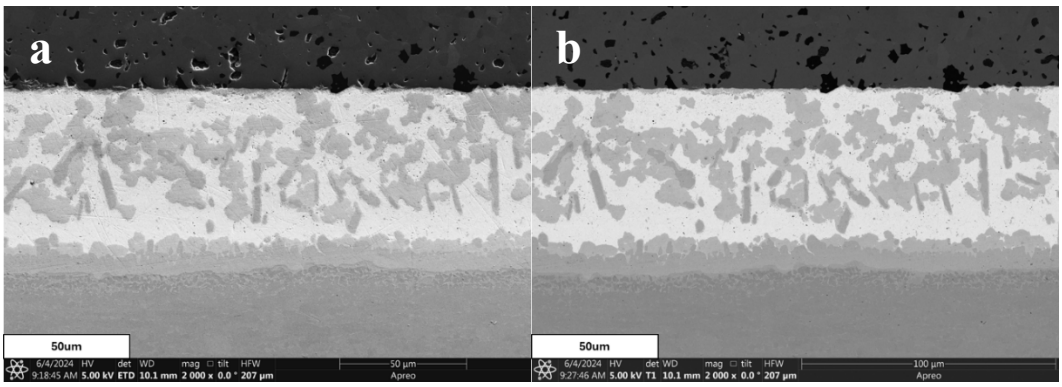

Figure 3. Overview of the SiC/InCuSil ABA/Ti-6Al-4V joint in cross section. a) Secondary-electron image and b) BSE image collected with an in-lens detector. The porous α-SiC occupies the top of the field, the α/β Ti-6Al-4V the bottom, and the Ag-rich braze zone, ~100 µm thick, lies between them.

The CBS detector resolves these phases considerably better than either the Everhart–Thornley or the in-lens backscatter detector (Figure 4). Summing all four CBS rings raises contrast across the whole field; using only the innermost A ring weights the image toward atomic number, brightening the high-Z constituents but saturating the SiC across the upper third of the frame. Higher-magnification A-ring images within the braze zone show the same phase assemblage along the Ti64 boundary as the wide field, confirming that the structure is continuous along the joint rather than a local feature.

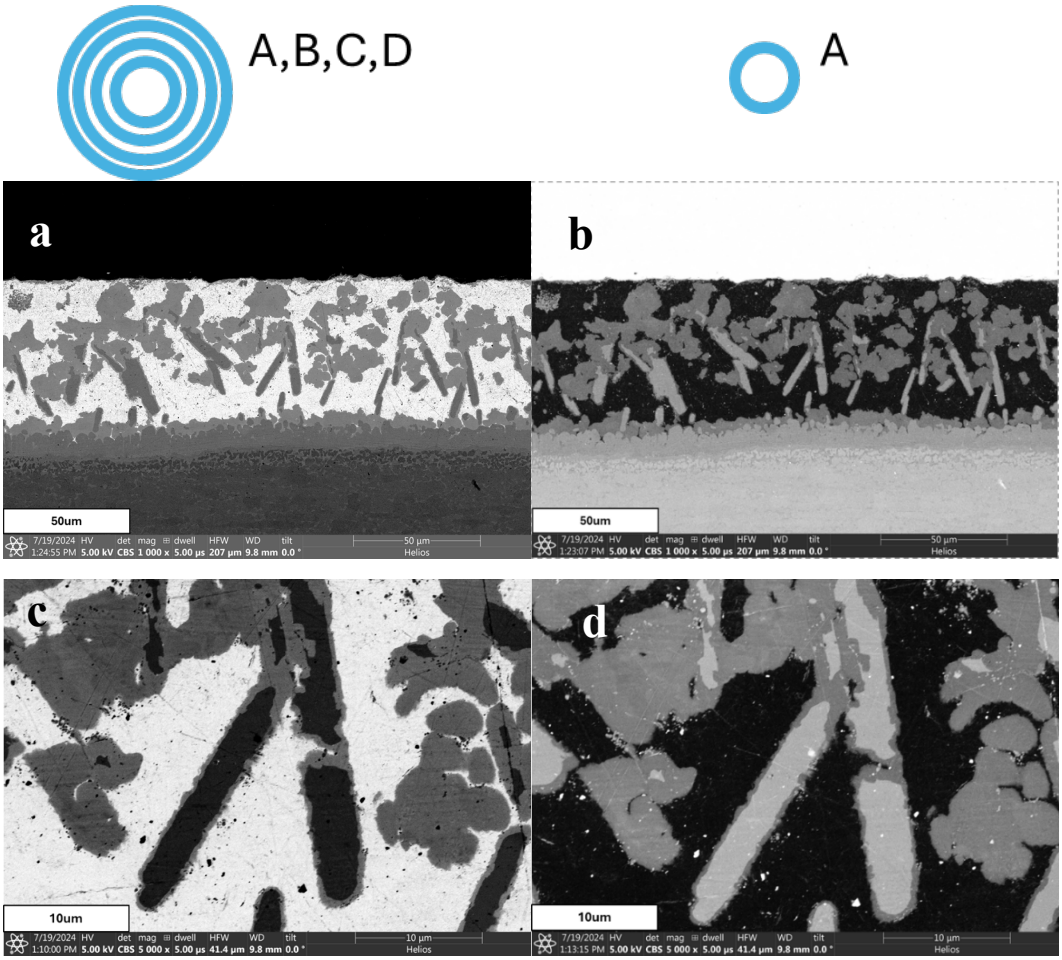

Figure 4. Concentric backscatter imaging of the same region. a) All four CBS rings summed; b) innermost A ring only, weighting the image toward atomic number and saturating in the SiC; and c,d) Higher-magnification A-ring views within the braze zone showing the same assemblage along the Ti64 boundary as the wide field.

The two boundaries of the interlayer are not equivalent, and this asymmetry is one of the more consequential observations in the report. Along the SiC–braze boundary (Figure 5a) adhesion is good and gaps occur only where the SiC itself is porous; the transition is abrupt, but it clearly includes one or more carbon-containing phases resident in the braze. Given the reactivity of the active titanium in the alloy, these phases are consistent with carbide-forming reactions reported for Ag-Cu-Ti active brazes,[1,2] although carbon is not easily resolved by XEDS in this system. Along the Ti64–braze boundary (Figure 5c), the transition is instead a graded region several micrometers wide in which existing phases have shifted composition and new phases have formed, melded together rather than stacked. Submicron dispersoids are distributed throughout the central braze region (Figure 5b).

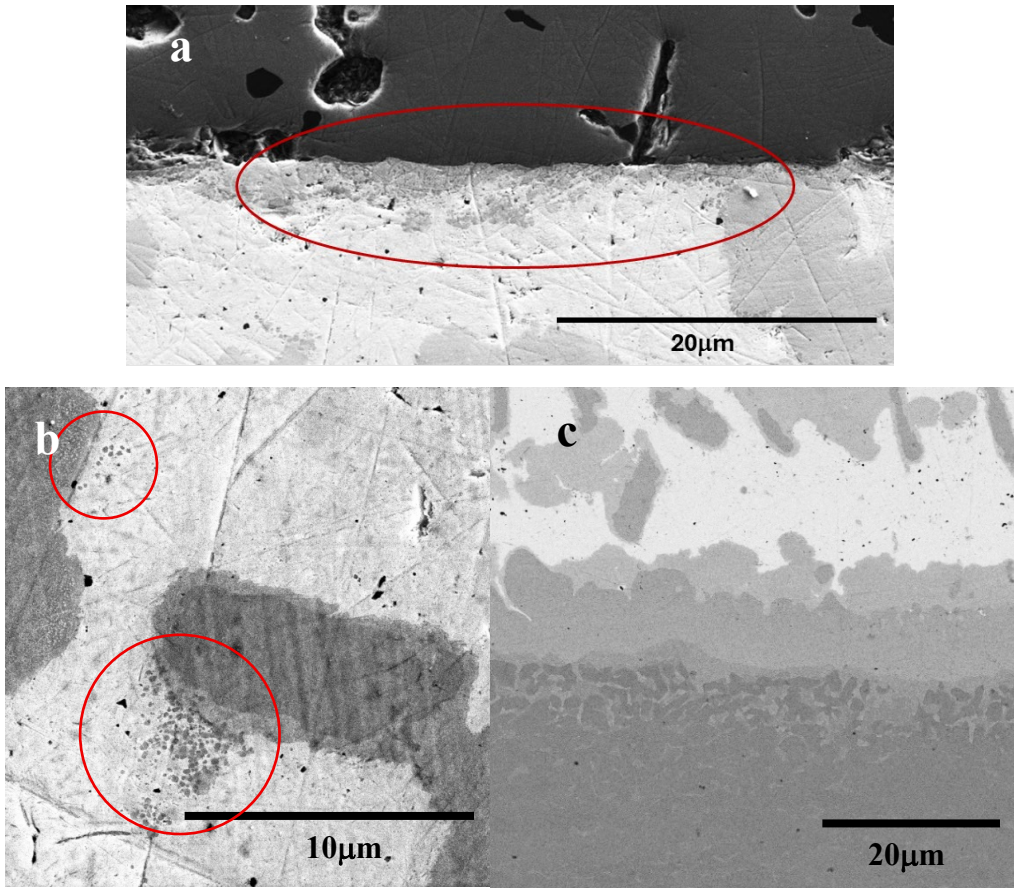

Figure 5. Reaction products within the braze zone. a) SiC–braze boundary, where adhesion is good and gaps occur only at SiC porosity. b) Submicron dispersoids distributed through the Ag-rich matrix. c) Ti64–braze boundary, a graded transition several micrometers wide containing shifted and newly formed phases.

Mechanically, this means the joint has one sharp interface and one diffuse one. Any clustering method applied across the interlayer will encounter a well-posed boundary at the ceramic and an ill-posed one at the metal and should be expected to perform differently at the two.

3.2 Elemental Distribution and Phase Chemistry

XEDS was collected over a wide field encompassing SiC, braze, and Ti64 as shown in Figure 6. Results show that silicon is not detected below the SiC layer, indicating that silicon does not migrate appreciably into the interlayer. Within the braze zone, Ag, Cu, and In dominate, as expected from the alloy composition. Two departures from that expectation are significant. First, a fraction of the Cu has segregated toward the Ti64. Second, Ti, V, and Al, have all infiltrated the braze zone, and the Ti and V maps show penetration well beyond the immediate boundary layer.

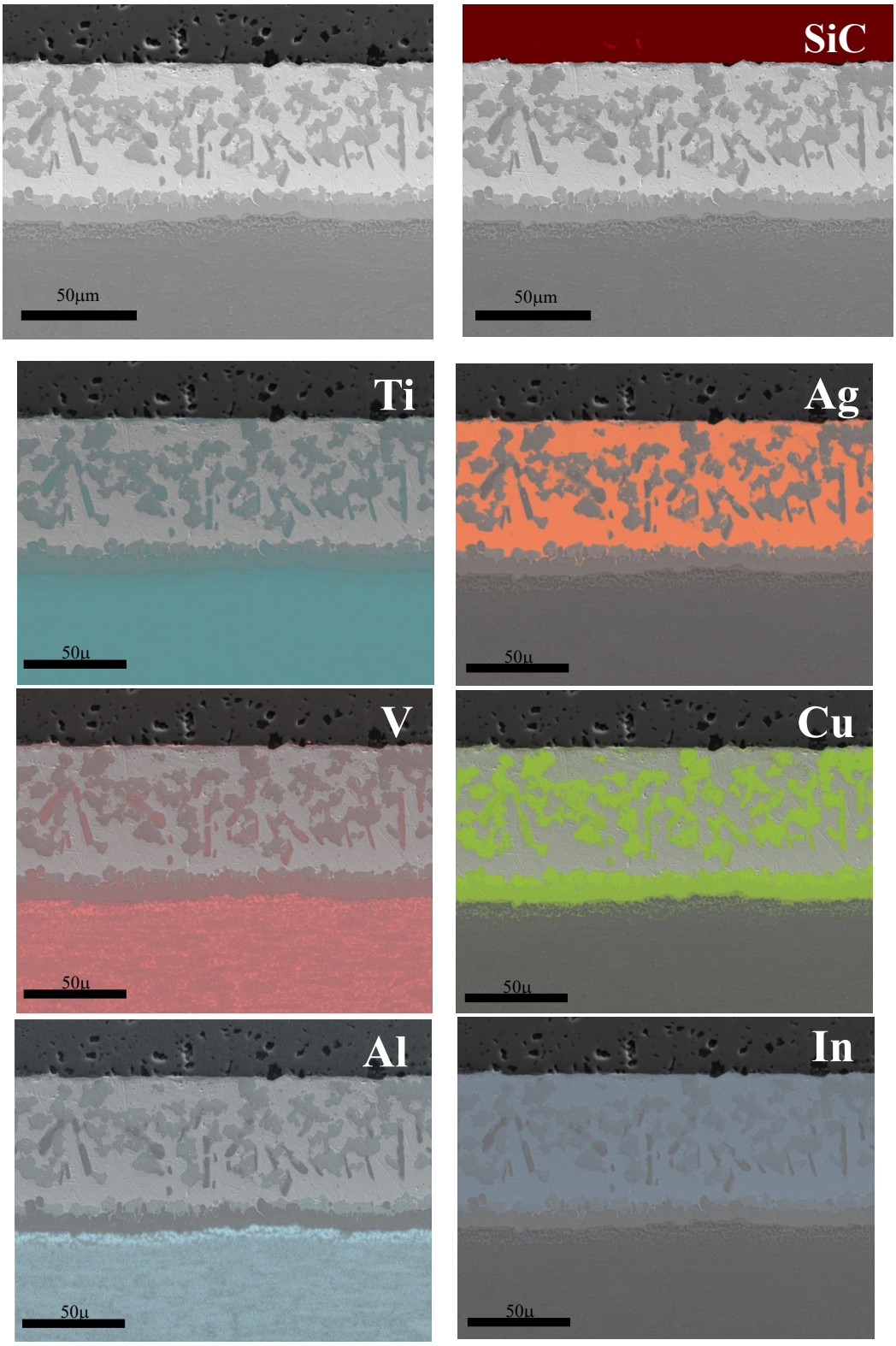

Figure 6. XEDS element maps for Ti, V, Al, Ag, Cu, and In. Top: wide field encompassing SiC, braze, and Ti64. Bottom: enlarged view of the braze zone. Silicon is not detected below the SiC layer. Ti, V, and Al, have infiltrated the braze zone; a fraction of the Cu has segregated toward the Ti64.

Standardless quantification of the phase maps (Figure 7) resolves three compositionally distinct reaction products. Compositions in the low- and high-magnification images of the braze-zone are compared in Table 3.

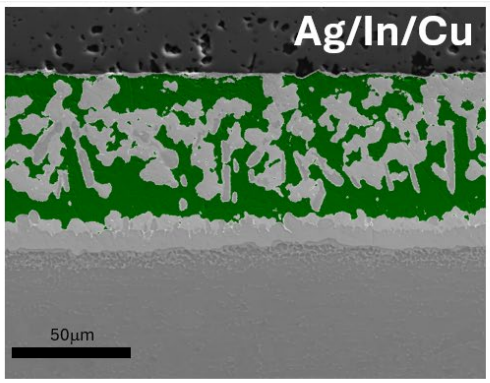

Ag	80.4%
In	12.0%
Cu	7.3%

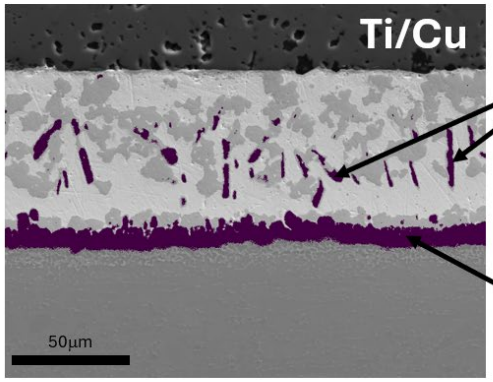

Cu	48.1%
Ti	48.1%
V	1.3%

Cu	50.2%
Ti	44.3%
V	2.2%

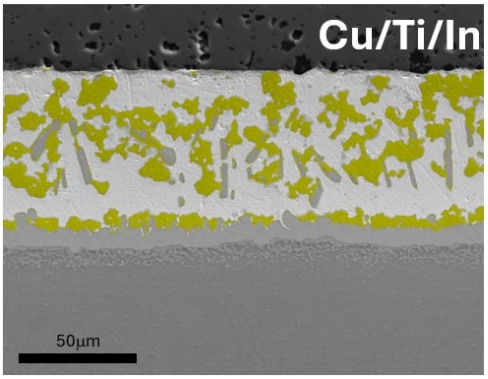

Cu	60.6%
Ti	25.3%
In	9.6%

Figure 7. XEDS phase maps and compositional quantification of the three reaction products, measured independently in the wide field and the enlarged braze-zone field. Compositions are compared in Table 3; agreement between the two fields is the basis for treating these as distinct phases rather than as samples of a continuous gradient.

Table 3. Standardless XEDS quantification of the three reaction products, measured independently at low and high magnification (wide field and in an enlarged braze zone, respectively). Elements below ~2 at% are omitted.

Phase	Low-magnification wide field (at%)	High-magnification enlarged braze zone (at%)	Assignment
Ag-rich matrix	80.4 Ag, 12.0 In, 7.3 Cu	76.8 Ag, 12.5 In, 8.5 Cu	AgInCu FCC (FCC no. 2)
Cu-Ti dispersoid	48.1 Cu, 48.1 Ti, 1.3 V	49.9 Cu, 44.7 Ti, 2.7 V	CuTi B11 intermetallic
Cu-Ti boundary layer	50.2 Cu, 44.3 Ti, 2.2 V	. . .	CuTi B11 intermetallic
Cu-Ti-In alloy	60.6 Cu, 25.3 Ti, 9.6 In	60.3 Cu, 25.4 Ti, 10.3 In	CuTiIn FCC (FCC no. 1)

Agreement between the two mapped fields supports the reproducibility of the compositional fingerprints, but it does not establish absolute analytical accuracy. Phase assignments are therefore based on the combined composition, morphology, and thermodynamic evidence.[19] Each phase is reproduced to within roughly 1 at%–4 at% on its major constituents, which is well within the accuracy expected of standardless quantification. That consistency supports treating these three compositions as genuine distinct phases rather than as sampling artifacts of a continuously graded region—an important point, because a graded interlayer and a multiphase interlayer make very different predictions about what clustering should recover.

XPS was performed on a PHI Versa Probe II. The XPS of the braze zone through an approximately 100-µm aperture detected oxygen, which XEDS could not resolve because of peak overlap in the low-energy region. Its concentration could not be determined. Oxygen at the interface is a plausible contributor to local embrittlement and one source of scatter in the indentation data, but on the present evidence nothing quantitative can be said, and oxygen accordingly plays no part in the following interpretation of results.

3.3 Thermodynamic Context

A pseudo-binary section computed between the InCuSil ABA and Ti-6Al-4V (Figure 8) shows the range of phases thermodynamically accessible as composition traverses the interlayer. Ordered Cu-Ti compounds, CuTi B11, $CuTi_3$, Cu_4Ti_3, Cu_3Ti_2, and Cu_4Ti, occupy a broad composition band at intermediate mole fraction, with FCC_A1 and BCC_B2 fields on either side and a CuIn θ phase near the braze-rich end. The liquidus rises from roughly 700 °C at the InCuSil end to approximately 1670 °C at the Ti64 end.

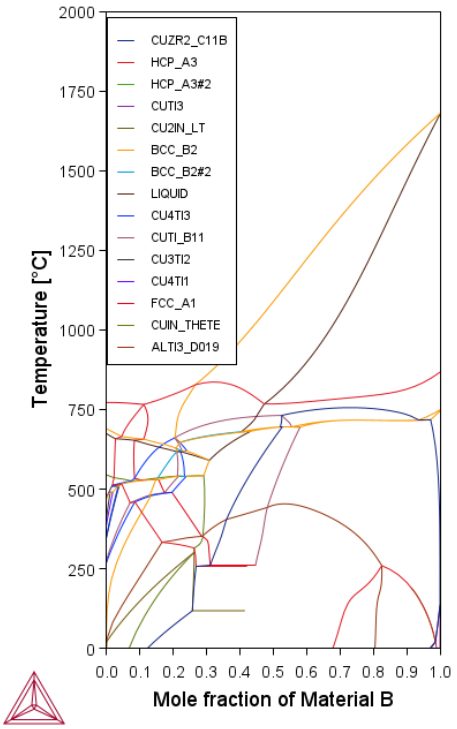

Figure 8. Pseudo-binary section computed between the InCuSil ABA and Ti-6Al-4V end members, showing the phases thermodynamically accessible as local composition traverses the interlayer. The section constrains which phases are possible; it does not predict phase fractions, since the braze cycle does not reach equilibrium.

This is consistent with the observed assemblage: CuTi B11 has roughly the same composition identified by XEDS as the boundary layer and as the dispersoids, and the FCC fields accommodate both the Ag-rich matrix and the Cu-Ti-In alloy. The section should be read as a constraint on which phases are possible, not as a prediction of what is present. A braze cycle typically does not reach equilibrium, the local composition is set by diffusion kinetics, and the section is a complex projection of a six-component system.

3.4 Five-Class Microstructural Model and Optical Reference Map

Combined interpretation of BSE contrast, XEDS measurements, and CALPHAD calculations supports a simplified five-class description of the joint cross section (Figure 9). The classes used throughout the subsequent analysis are as follows:

- **0: SiC ceramic:** porous SiC substrate
- **1: Ti-6Al-4V:** α/β titanium substrate

- **2: CuTi intermetallic:** approximately 50Cu-44Ti-2Ag-2V-1.5In; present as a thin, nearly continuous layer along the Ti-6Al-4V boundary and as elongated constituents within the braze
- **3: CuTiIn alloy (FCC no. 1):** approximately 60Cu-25Ti-10In-2Ag-2Al.
- **4: AgInCu matrix alloy (FCC no. 2):** approximately 80Ag-12In-7Cu; the continuous matrix of the braze interlayer

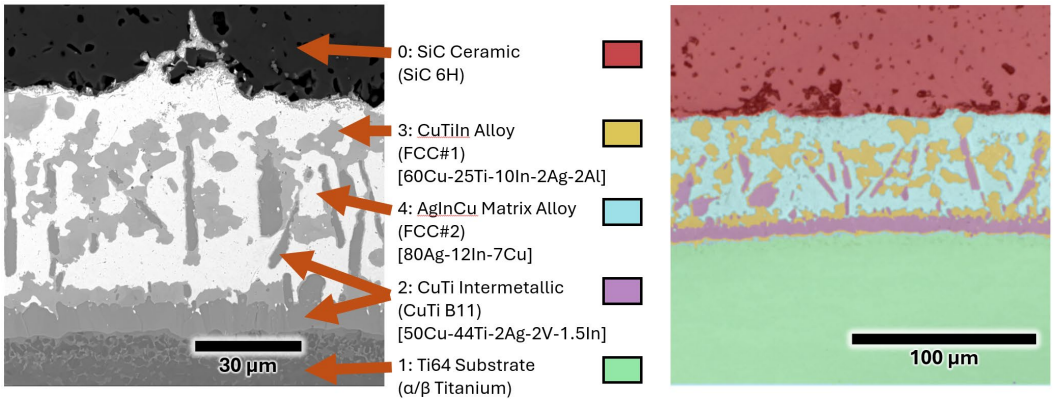

Figure 9. Simplified five-class microstructural model of the SiC/Ti-6Al-4V joint. Left: BSE image showing the assigned constituents and approximate compositions determined from the combined microstructural analysis. Right: corresponding architecture represented by optical image segmentation.

Trainable WEKA Segmentation reproduced the principal spatial features of this model in the optical micrographs (Figure 10). A classifier trained on a separate region identified the SiC and Ti-6Al-4V end members, the CuTi-rich boundary region, and the two principal regions within the braze. The resulting segmentation also preserved the elongated morphology of the CuTi-rich constituents and the interpenetrating morphology of the braze constituents.

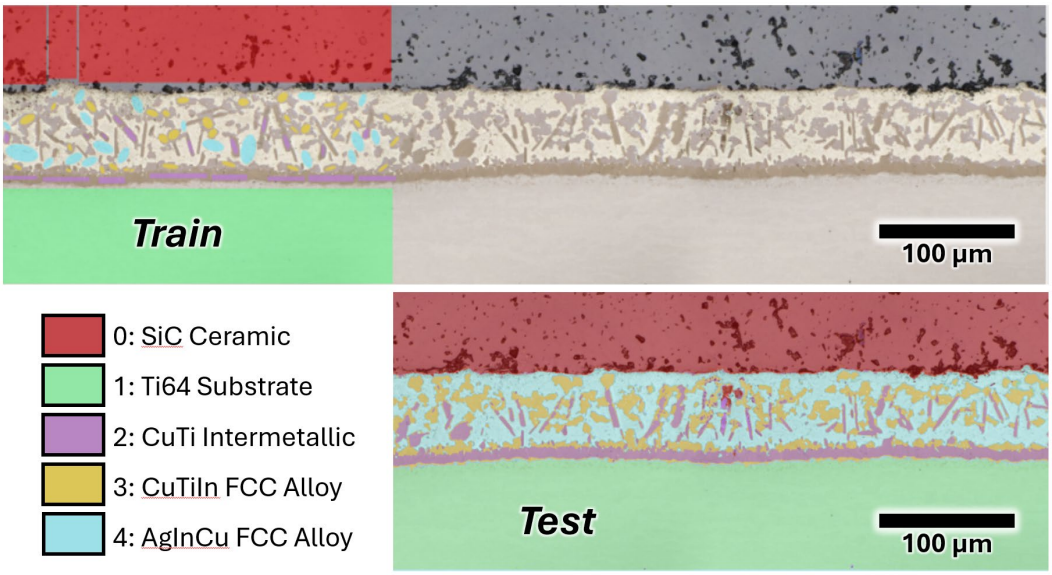

Figure 10. Supervised optical segmentation of the polished joint cross section using Trainable WEKA Segmentation. (top) Manually labeled training region used to establish the five optical classes; (bottom) predicted classes within the spatially separate region containing the nanoindentation arrays. The resulting map provides the microstructural reference used for spatial comparison with the indentation measurements.

The segmentation provides a practical link between the microstructural characterization and the mechanical measurements. Following image registration, each indent can be associated with the optical class located at its center and compared with its independently determined mechanical grouping. The optical classification is not used to determine phase chemistry or to train the mechanical clustering. Phase interpretation remains based on the combined microscopy, XEDS, and thermodynamic analysis described above.

Because the optical classes are distinguished by image contrast and morphology, the segmentation is best regarded as a spatial reference map rather than an independent measurement of phase identity. This distinction is most important at constituent boundaries and within narrow reaction layers, where optical classification can assign a discrete class even though the indentation interaction volume samples more than one constituent. The segmentation is therefore used to evaluate spatial correspondence between the microstructural and mechanical maps, rather than as absolute ground truth.

3.5 Mechanical Response of the Monolithic Regions

The controlled measurements in the monolithic SiC and Ti-6Al-4V regions provide reference responses for interpreting the NanoBlitz arrays. This comparison is important because the fixed-load, high-rate NanoBlitz measurements are optimized for rapid spatial mapping rather than direct equivalence with conventional

nanoindentation. The selected loads limit overlap between neighboring indents in the more compliant regions of the joint but consequently produce much smaller impressions in the harder constituents. These shallow measurements may be more sensitive to indentation size effects and surface condition. In addition, the higher indentation strain rate used during NanoBlitz testing can alter the measured hardness of rate-sensitive materials. The controlled monolithic measurements therefore provide a useful reference for determining whether the mechanically identified populations exhibit responses consistent with the corresponding end members, without requiring the array-derived properties to reproduce the reference values exactly.

Residual impressions in the two end members differ qualitatively, as shown in Figure 11. In SiC, pronounced radial cracks extend from the corners of the Berkovich impression into the surrounding material, consistent with brittle fracture under concentrated contact loading. In Ti-6Al-4V, radial cracking is absent; instead, substantial pile-up develops around the impression, indicating localized plastic flow. Because pile-up increases the actual contact area relative to that inferred from the load-displacement response, conventional indentation analysis can underestimate contact area and consequently overestimate hardness and modulus.[26,28]

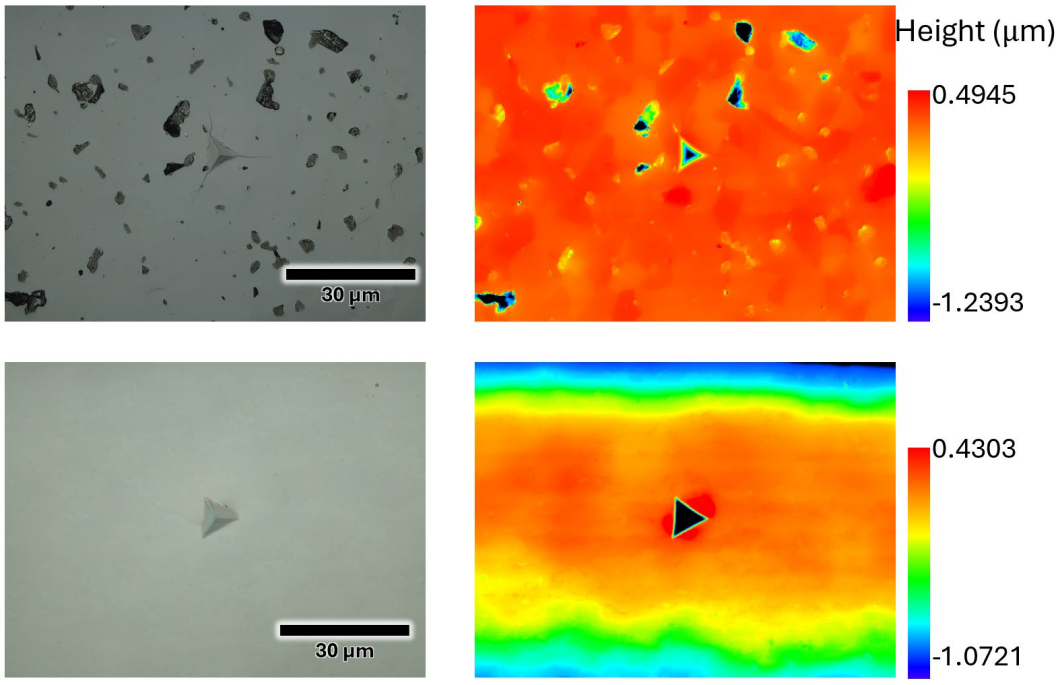

Figure 11. Residual Berkovich impressions associated with the bulk response. Top: SiC, showing radial cracking from the impression corners. Bottom: Ti64, showing pile-up and no cracking. Optical images at left, profilometric height maps at right. Note that the two height scales differ.

Reference properties for both end members are given in Table 4.

Table 4. Bulk indentation properties of the monolithic regions, measured at least 1 mm from the interface. Values are mean ± standard deviation over 10 tests in each material.

Sample	Hardness (GPa)	Modulus (GPa)	P_max (mN)	Reporting depth (nm)
SiC	30.94 ± 0.98	495.74 ± 3.97	999.69 ± 0.24	1250.58 ± 10.77
Ti64	4.28 ± 0.10	131.58 ± 1.20	845.88 ± 12.87	2134.17 ± 11.95

These values are the anchors for everything that follows. Any cluster whose hardness and modulus fall near 31 and 496 GPa can be assigned to SiC with confidence, and any cluster near 4.3 and 132 GPa to Ti64. Clusters that fall between them require interpretation.

3.5.1 Indentation Size Effect

Nix–Gao[23] fits to the depth-resolved hardness data (Figure 12) give the parameters in Table 5.

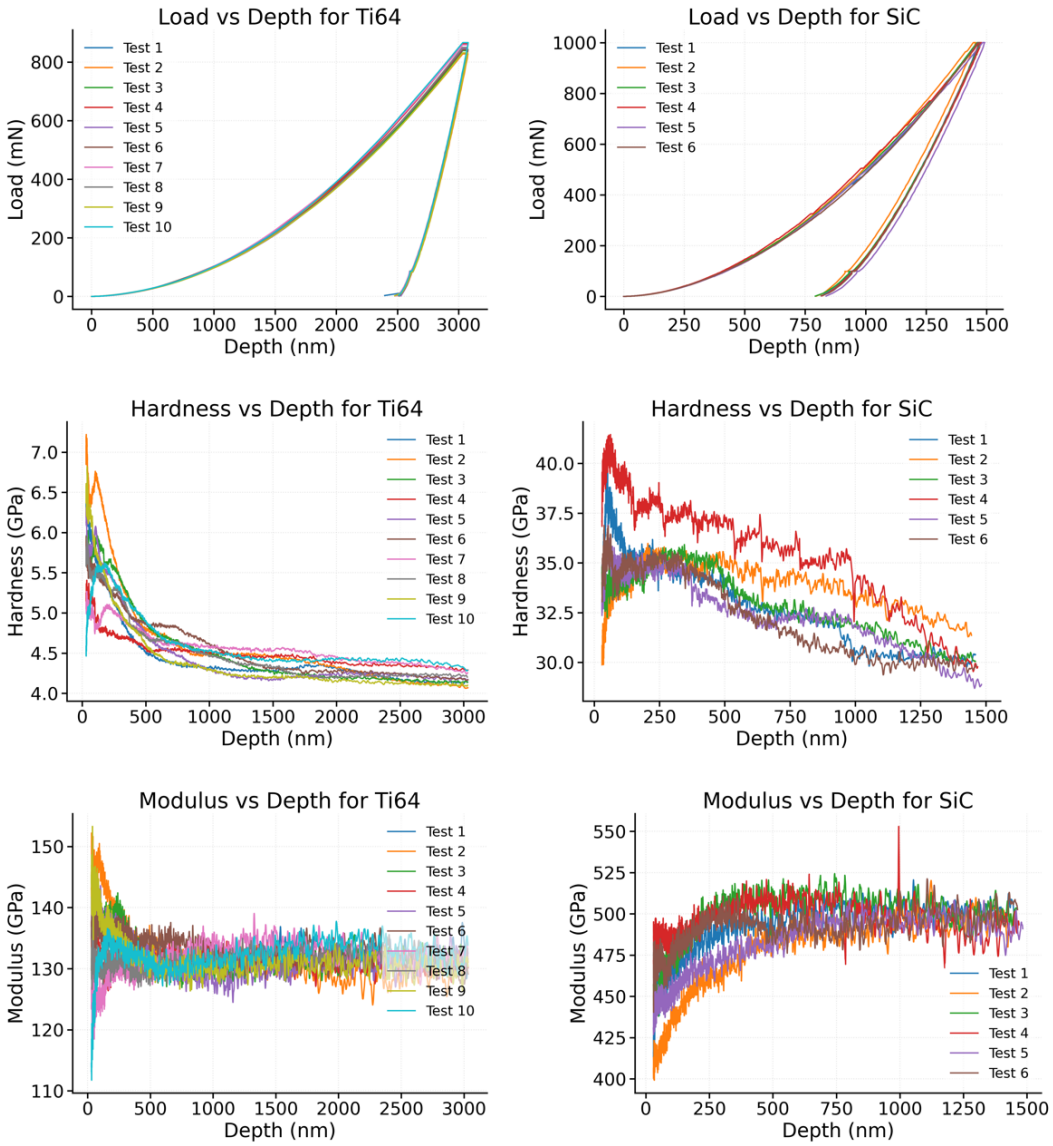

Figure 12. Indentation size effect in Ti64 (left) and SiC (right). Top: measured hardness against depth with the shallow-depth cutoff marked. Middle: H^2 against $1/h$ with the Nix–Gao fit. Bottom: fit residuals. Residual structure is systematic in both materials and discontinuous in SiC, which is why only H_0 and not h^* is carried forward.

Table 5. Nix–Gao indentation size effect parameters, fitted above the stated shallow-depth cutoff.

Material	H_0 (GPa)	h^* (μm)	Fit cutoff (μm)	Bulk H from Table 4 (GPa)
Ti64	4.272 ± 0.157	0.117 ± 0.107	0.29	4.28 ± 0.10
SiC	30.04 ± 3.53	0.233 ± 0.123	0.30	30.94 ± 0.98

The asymptotic hardness values agree closely with the independently measured bulk hardness in both materials (4.272 against 4.28 GPa for Ti64, and 30.04 against 30.94 GPa for SiC), which is a genuine internal consistency check on the indentation calibration.

The characteristic lengths are a different matter and should be reported with an explicit caveat. The uncertainty on h^* is 91% of its value for Ti64 and 53% for SiC. Neither is determined well enough to support a physical argument about the spatial extent of gradient hardening. The residual plots explain why: for Ti64, the residuals form a smooth arch spanning roughly ±1.5 GPa² rather than scattering about zero, and for SiC they show large systematic excursions of ±100 GPa² together with a sharp discontinuity near a fitted H^2 of 1300 GPa². A Nix–Gao model assumes a single population of geometrically necessary dislocations accommodating the indentation strain gradient[22,23]; in SiC, where plasticity is accompanied by cracking, that assumption is not obviously valid, and the residual structure suggests it is not. The fits should be used to obtain H_0 and to demonstrate that the arrays operate in a size-effect-affected regime. They should not be used to argue for a particular value of h^*.

The practical consequence for the array data is direct. Both NanoBlitz arrays produce contact depths in the 150- to 700-nm range, which is close to h^* for both materials. Array hardness values will therefore sit systematically above the bulk values in Table 4, and the offset will differ between phases because h^* differs between phases. This is not an error to be corrected away; it is a real effect that must be stated when array-derived and quasi-static hardness values appear in the same discussion.

3.5.2 Strain-Rate Sensitivity

Strain-rate jump tests (Figure 13) were used to determine SRS and given $m = 0.0173 \pm 0.0068$ for Ti64 and $m = 0.0168 \pm 0.0102$ for SiC. The measured Ti64 value is of the same order as indentation strain-rate sensitivities reported for dual-phase titanium alloys and Ti-6Al-4V. Differences in microstructure, loading history, and strain-rate range prevent direct numerical comparison.[29,30]

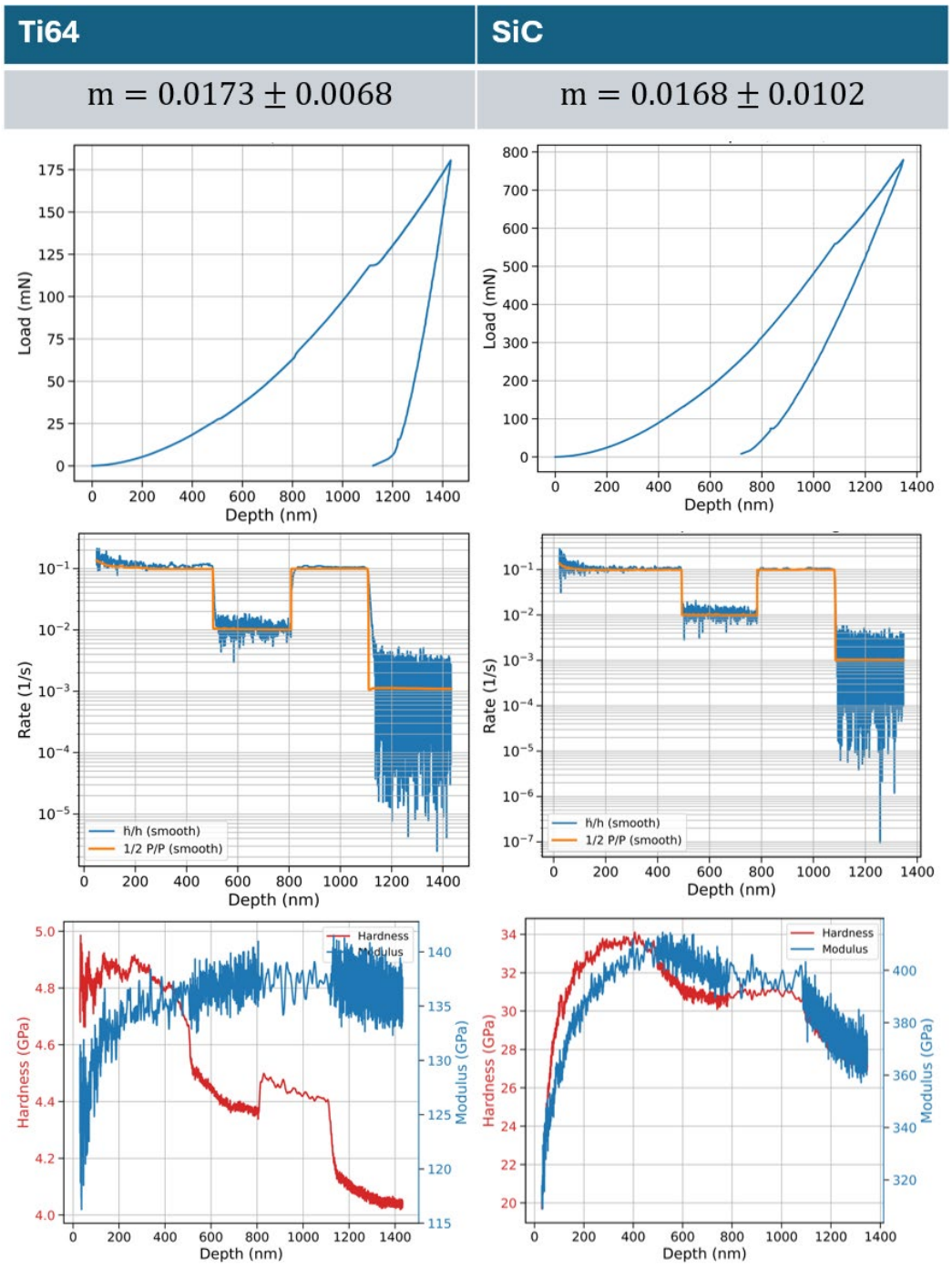

Figure 13. Strain-rate jump testing of the monolithic end members (SiC and Ti64). Top: load (P), depth (h) response. Middle: prescribed $\dot{P}/P$ against apparent $\dot{h}/h$ indentation strain rate. Bottom: hardness (H) and modulus (E) against depth through the rate sequence. The monotonic hardness decline in SiC is dominated by the size effect and by cracking, not by indentation strain rate.

The large standard deviation observed for the SiC provides a strong indication that this specific measurement of SRS is unreliable. It is statistically indistinguishable from the Ti64 value, and its uncertainty spans zero (within 1.7 standard deviations).

Room-temperature SiC is not expected to exhibit measurable indentation rate sensitivity by a dislocation mechanism; the hardness–depth trace for SiC instead shows a monotonic decline through the entire test that is dominated by the indentation size effect and by progressive cracking, and the extrapolation procedure of Equation 3 cannot cleanly separate that decline from a rate response. The honest statement is that SiC shows no resolvable strain-rate sensitivity under these conditions, and that the fitted value is an artifact of applying a metal-oriented analysis to a brittle material.

The Ti64 measurements indicate a small but resolvable strain-rate response. The SiC experiment does not resolve intrinsic strain-rate sensitivity because the hardness response is confounded by indentation size effects and cracking. While it could be possible to use SRS as a feature to drive segmentation, large indentation depths are typically required to measure SRS from a single indent, which extends the sampling volume and reduces the spatial resolution of indentation tests.

3.6 Interface Characterization by NanoBlitz Array

Both arrays were placed inside the region imaged before indentation, so every indent coordinate can be referred to pristine microstructure (see Figure 2). The 10-mN array occupies the left (blue) portion of the ROI and the 20-mN array the right (red); the two footprints do not overlap, which means the two loads sample adjacent but not identical microstructure. That is a limitation on how directly the two partitions can be compared and it is carried through every comparison below.

Marginal distributions of the four measured channels are shown for both arrays in Figure 14. Every channel is bimodal, and the bimodality has the same origin in each case: a large low-hardness, low-modulus population comprising the metal substrate and the entire braze zone, and a small high-hardness, high-modulus population corresponding to SiC. In the 20-mN array, the hardness distribution shows a dominant mode below about 6 GPa carrying roughly 220 of 376 indents and a secondary population between 30 and 40 GPa carrying perhaps 60; the modulus distribution mirrors it with modes near 130–150 and 400–500 GPa. The 10-mN array behaves the same way at lower absolute stiffness, with contact stiffness spanning 0.15–0.32 MN/m against 0.22–0.48 MN/m at 20 mN.

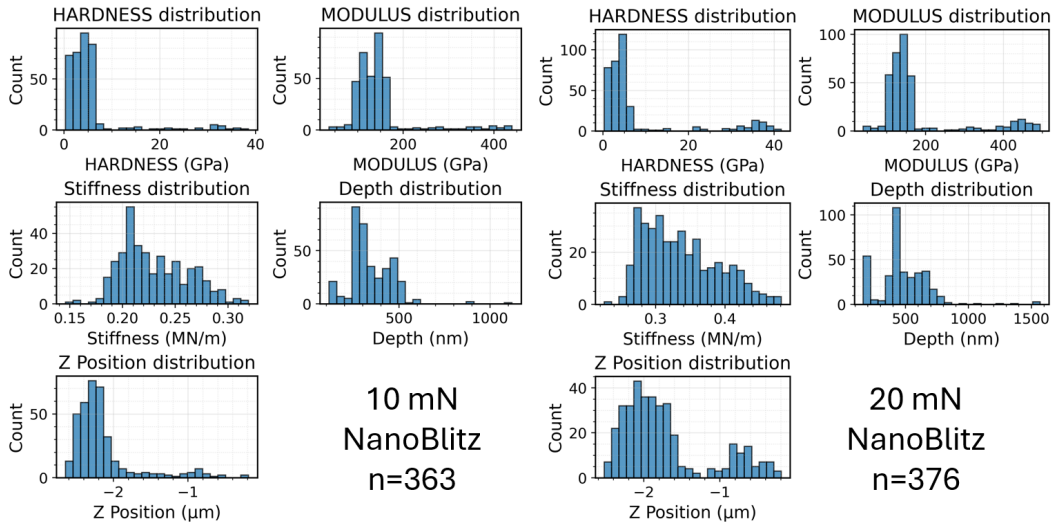

Figure 14. Marginal distributions of hardness, modulus, contact stiffness, depth, and surface height for the 10-mN (n = 363) and 20-mN (n = 376) arrays. Every channel is bimodal, separating SiC from the metal and braze; the individual braze phases are not resolved in any single channel. The depth tails beyond 1000 nm are the result of poorly supported indents (e.g., porosity).

The important negative result is that the braze phases are not separately visible in any single-channel histogram. The interlayer constituents do not form visually separable modes in the individual property distributions. Phase assignment from univariate deconvolution alone would therefore be poorly constrained, particularly where responses overlap or individual indents sample multiple constituents.[8,11] This is precisely the situation that motivates multivariate clustering: the phases are distinguishable only through the joint distribution of hardness, modulus, stiffness, and depth, not through any one of them.

The depth channel additionally reveals the contamination problem. Both arrays show a distinct shallow spike near 150–200 nm (indents on SiC, which resists penetration) and a long tail extending past 1000 nm and, in the 20-mN array, past 1500 nm. Indents reaching a depth of 1500 nm at 20 mN correspond to an apparent hardness well below 1 GPa, which no phase in this system is expected to possess. These are indents that landed in porosity, on the edge of a pore, or in a region already cracked by a neighboring indent. They constitute a small but nonnegligible fraction of both arrays and their handling greatly determines what the clustering returns.

3.7 Feature Correlation and Selection of the Number of Clusters

Pearson correlations among the analyzed variables in the 20-mN array (Figure 15) show substantial redundancy. Hardness and modulus correlate at r = 0.98. Vickers hardness correlates with hardness at r = 1.00, as it must, since it is a unit conversion.

The logarithmic transforms ln(H) and ln(E) correlate with their untransformed counterparts at r = 0.91–0.97 and with each other at r = 0.96. Depth correlates with ln(H) at r = −0.92 and with hardness at r = −0.70, contact stiffness with depth at r = 0.66 and with hardness at r = −0.54.

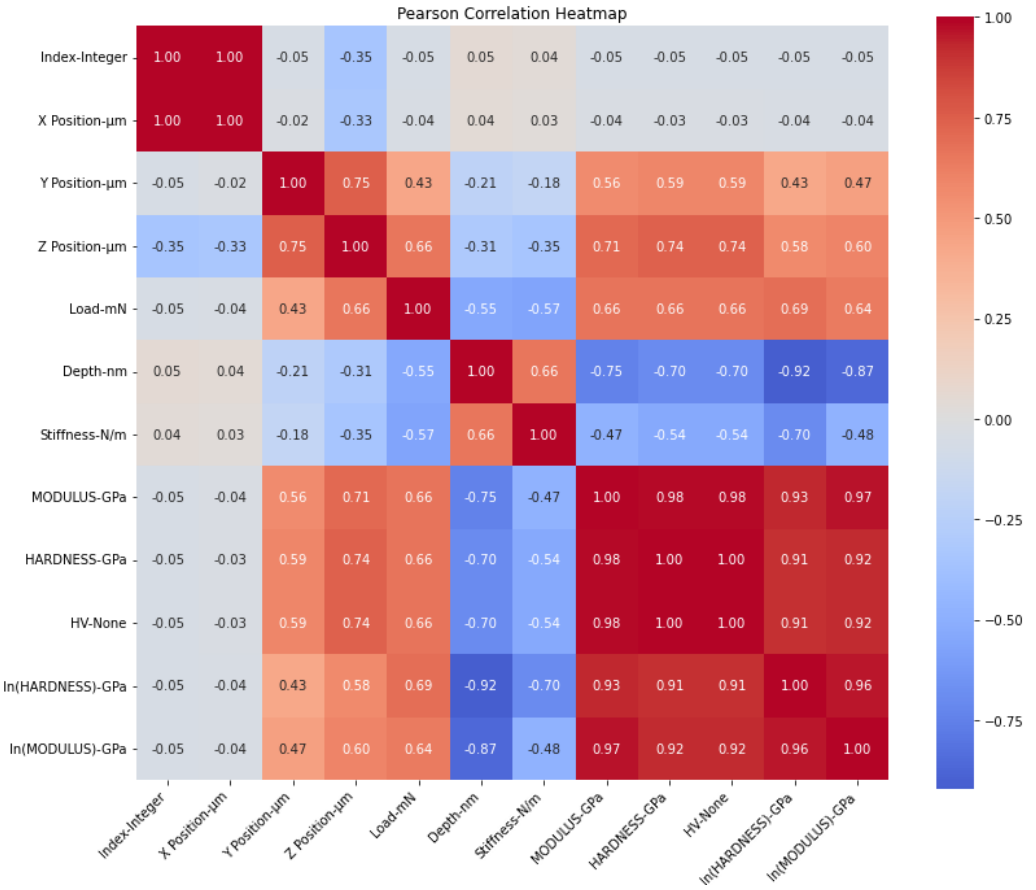

Figure 15. Pearson correlation matrix of the analyzed variables for the 20-mN array. Hardness and modulus correlate at r = 0.98; the derived quantities HV, ln(H) and ln(E) are largely redundant with their sources. Lateral position X correlates with nothing at $|r| \leq 0.05$.

This matrix is what justifies the compact feature set of ln(H), ln(E), and Z. Hardness, Vickers hardness, ln(H), modulus, and ln(E) are effectively two independent quantities, not five; retaining one hardness-like and one modulus-like variable is sufficient, and the logarithmic forms are preferred because the property distributions of Figure 14 are heavy-tailed. The Z position (surface height) correlates with modulus at r = 0.71 and with hardness at r = 0.74, strongly enough to carry phase information. However, the correlation is not perfect and the physical mechanism that produces this height difference is differential polishing wear: phases with higher wear resistance protrude from the surrounding material after the extended polishing. Therefore, Z functions as an independent slow-speed wear probe of each site and provides a surrogate for wear resistance. Lateral position X

correlates with nothing at $|r| \leq 0.05$, as expected (the joint runs along X, so composition does not vary with it) and X and Y were accordingly excluded from clustering. The same correlation structure appears in the 10-mN array, but this was not a focus of this report. Cluster-number diagnostics for both arrays are shown in Figure 16, with values listed in Table 6.

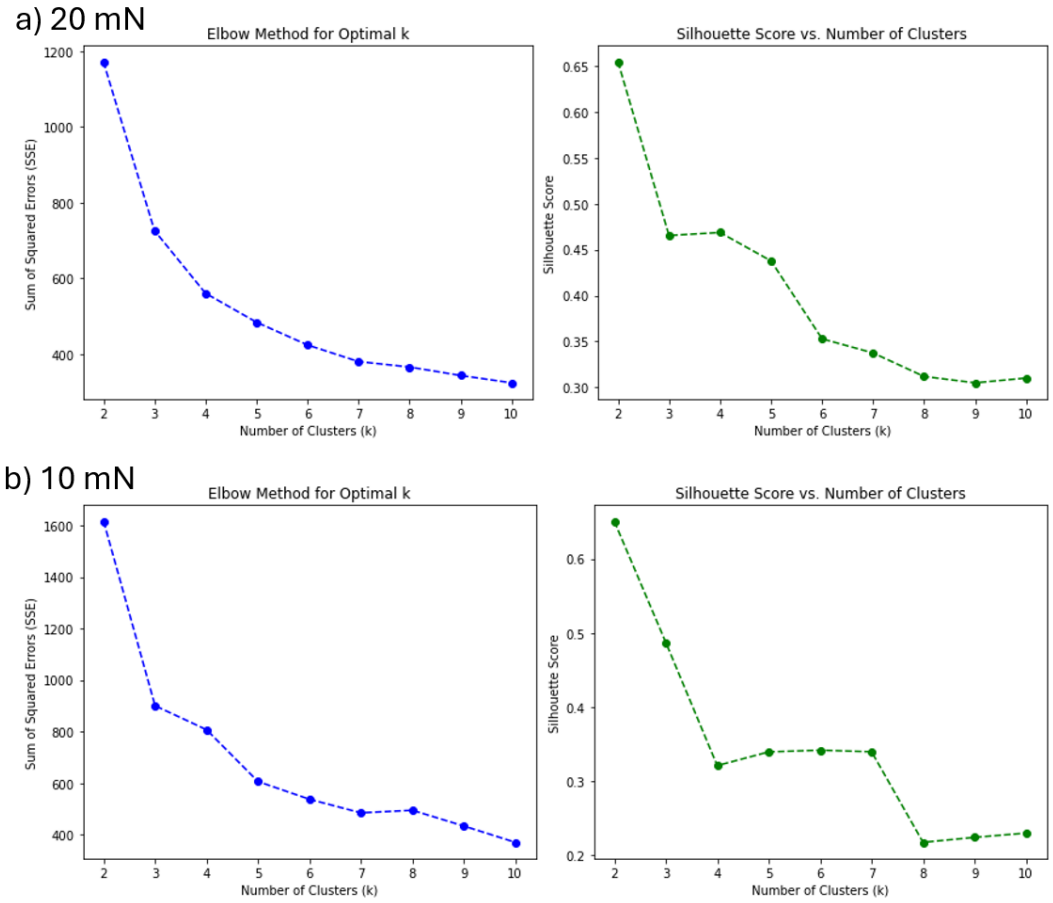

Figure 16. Selection of the number of clusters. Within-cluster sum of squares and average silhouette width for k = 2 – 10, shown for a) the 20-mN array and b) the 10-mN array. Both arrays favor k = 2 and support k = 3; neither shows a local optimum at k = 5.

Table 6. Average silhouette width against number of clusters for both arrays.

k	Silhouette, 20 mN	Silhouette, 10 mN
2	0.65	0.65
3	0.47	0.49
4	0.47	0.32
5	0.44	0.34
6	0.35	0.34
7	0.34	0.34
8	0.31	0.22

Both arrays show a global maximum at k = 2 with a silhouette of 0.65, which represents a well-separated partition. It is also the least interesting one—it separates a 30-GPa ceramic from everything metallic, a distinction that hardly requires instrumented indentation to draw. Its value is as a calibration check, the measurement, the feature set, and both algorithms all recover the one partition that is known with certainty to exist. Both arrays drop to roughly 0.47–0.49 at k = 3, still a reasonable structure. Beyond that the two arrays diverge in detail (the 20-mN array holds near 0.44–0.47 through k = 4 – 5 while the 10-mN array falls to a plateau near 0.33) but neither shows any local maximum at k = 5. The elbow criterion tells the same story: the within-cluster sum of squares falls steeply from k = 2 to k = 3 in both arrays and flattens thereafter, with only a weak secondary break near k = 5 in the 10-mN data.

This is a known behavior of internal validity indices rather than a verdict on the material: silhouette and elbow reward separation, not scientific interest, and in a dataset containing one mechanically extreme class they are dominated by the trivial split.[31] The analysis proceeds past k = 2 precisely because the best-scoring partition is the least informative one. The interlayer structure that is the object of study appears at higher k at lower silhouette, which is expected, since the reaction products differ from one another far less than any of them differs from SiC. A five-cluster description is nevertheless not selected by the mechanical data; it is imposed by the microscopic investigation discussed previously.

3.8 Mechanical Partitioning of the 20-mN Array

K-medoid partitions of the 20-mN array at k = 5 are shown in Figure 17, with the spatial cluster map registered against the optical micrograph and the corresponding property means in the accompanying scatter panels. Approximate cluster locations in feature space are summarized in Table 7.

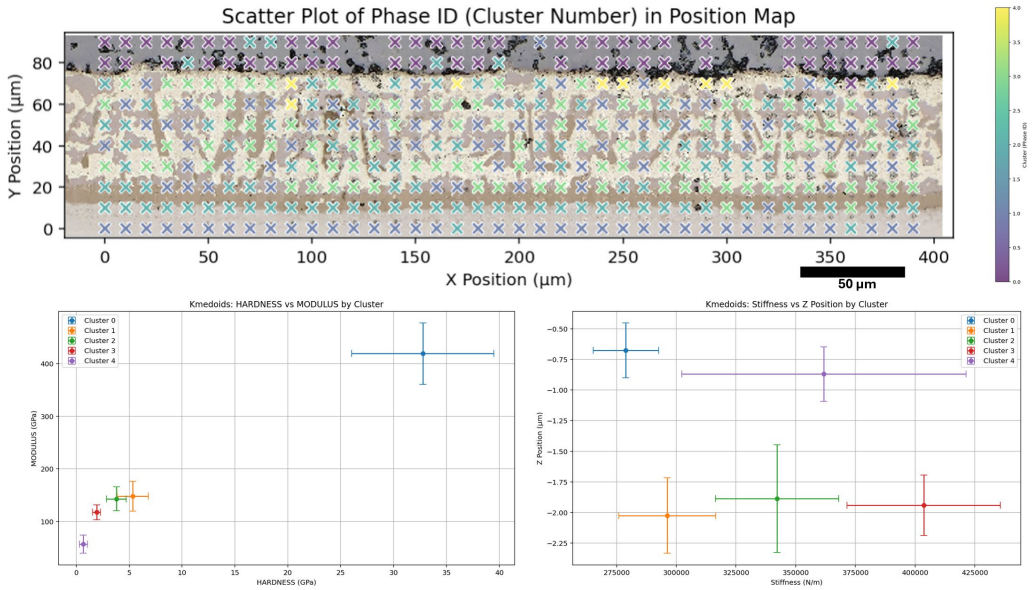

Figure 17. K-medoids partition of the 20-mN array at k = 5. Cluster map registered against the optical micrograph, with cluster means and standard deviations in hardness–modulus, and stiffness–height projections. Cluster 4 corresponds to anomalously deep, compliant indents attributed to SiC porosity rather than to a phase.

Table 7. Approximate k-medoids cluster centers for the 20-mN array at k = 5. Note that hardness, modulus, and *Z* entered the clustering (as ln *H*, ln *E*, *Z*); stiffness and depth are shown for interpretation but did not drive the partition.

Cluster	*H* (GPa)	*E* (GPa)	Stiffness (kN/m)	Depth (nm)	*Z* (µm)	Interpretation
0	33	420	278	180	−0.8	α-SiC
1	5.5	150	300	410	−2.0	Ti64 and stiff braze constituents
2	4.0	143	345	470	−1.85	Braze matrix
3	2.2	118	405	650	−1.95	Soft braze/boundary-affected indents
4	0.5	50	365	1220	−0.9	Artifact, porosity

The 20-mN array demonstrates that the mechanically heterogeneous structure of the joint can be recovered from the indentation measurements without using lateral position as a clustering variable. Cluster 0 is readily associated with SiC. Its mean hardness and modulus are approximately 33 and 420 GPa, respectively, and the cluster occupies the SiC region of the registered micrograph. The hardness is slightly greater than the reference value of 30.94 GPa, consistent with measurements made within the indentation-size-effect regime.[23] The lower modulus relative to the reference value of 495.74 GPa likely reflects some combination of local porosity and measurements influenced by adjacent microstructural features. Although porosity and early fracture would be expected to reduce both hardness and modulus, the elevated hardness indicates that the

indentation size effect associated with the shallow 20-mN indents (median recorded depth of ~180 nm) likely offsets these effects and shifts the measured hardness above the reference value. These effects are difficult to separate within a high-speed array and caution against treating cluster means as intrinsic phase properties.

Clusters 1 through 3 form a systematic progression of decreasing hardness and modulus with increasing penetration depth. More importantly, these populations occupy contiguous regions approximately parallel to the joint. Because X and Y position were excluded from the clustering variables, this spatial organization was not imposed by the analysis. Mechanically similar measurements are spatially associated because the underlying microstructure is spatially organized. Cluster 1 is associated primarily with Ti-6Al-4V, while Clusters 2 and 3 occupy different regions of the braze interlayer. The important result is therefore not the precise cluster label, but the observation that the approximately 100-μm interlayer cannot be described adequately as a single mechanically homogeneous material.

Cluster 4 has a substantially different character. Its mean hardness and modulus are approximately 0.5 and 50 GPa, respectively, while its mean contact depth approaches 1.2 μm. These values are inconsistent with the phases identified by microscopy and compositional analysis. The spatial location of these measurements, together with the porosity observed in the SiC and the long penetration-depth tail in Figure 14, indicates that this population is dominated by pore-affected or otherwise poorly supported indents. Similar effects of porosity, roughness, and mixed sampling have been reported in high-density nanoindentation maps.[8]

This population is therefore not interpreted as an additional material phase. Its isolation is nevertheless useful experimentally. Rather than requiring aggressive statistical filtering, k-medoids separate a population of unusual measurements while retaining them in the dataset. Because a medoid is an observed indent rather than a calculated centroid, its representative measurement can also be returned to the load-displacement record and the corresponding microstructural location.[15,16] This is a practical advantage of k-medoids for experimental mapping, but it does not imply that every resulting cluster corresponds to a physical phase.

3.9 Comparison with K-means

K-means was applied to the same standardized variables to determine whether the major interpretations depended on the partitioning method. At k = 2, k-means and k-medoids produce nearly identical partitions of the 20-mN array. Both separate the SiC-rich region from the remainder of the joint, and the resulting boundary closely follows the SiC-braze interface. The strong agreement indicates that this

division is inherent to the mechanical data rather than a consequence of the clustering objective.

At k = 5, the comparison becomes more informative. Both algorithms continue to identify the SiC region, but their assignments within the braze become substantially less consistent. The divergence should not be interpreted simply as one algorithm succeeding and the other failing. Instead, it indicates that the mechanical populations within the interlayer overlap sufficiently that the detailed partition becomes method-sensitive. K-medoids is preferable for the present analysis because extreme observations exert less influence on the representative values and because each medoid remains an experimentally traceable indent. Where the populations are well separated, however, the two methods reach essentially the same result. The k-means cluster partitions and averages are shown in Figure 18.

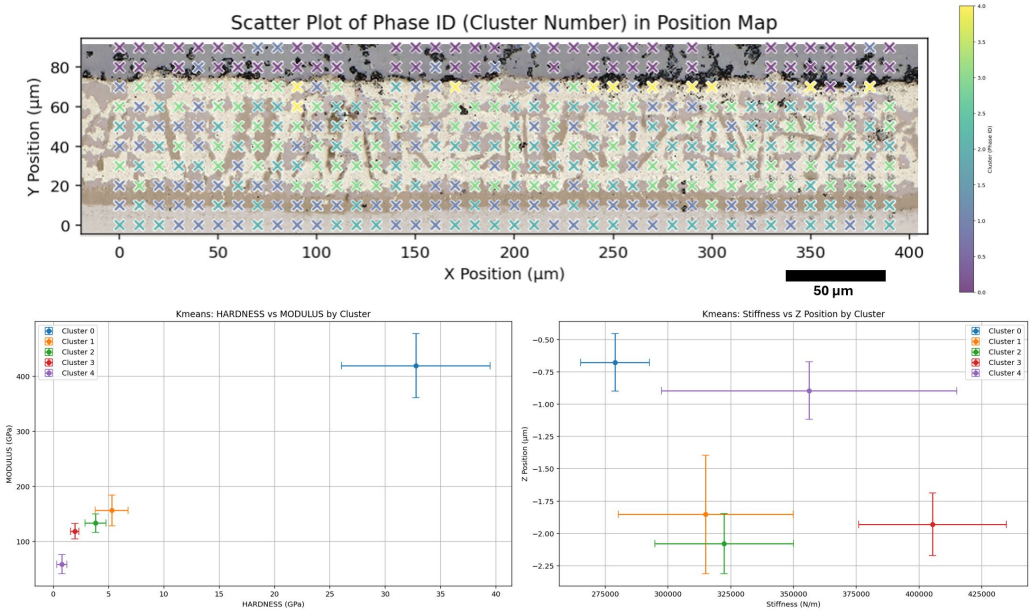

Figure 18. K-means partitions at k = 5 for the 20-mN array.

A direct comparison between k-means and k-medoids clustering results are shown in a spatial map in Figure 19. The clustering results are consistent for k = 2, effectively distinguishing between ceramic and metallic phases; however, the populations diverge significantly at k = 5. The k-medoids technique does a better job of highlighting the banded structure of reaction products between the Ti64 substrate and the braze. Cluster numbers are algorithm-specific and should not be compared directly without matching the corresponding populations. Rank ordering of hardness or modulus could be used to improve correlations between different clustering algorithms.

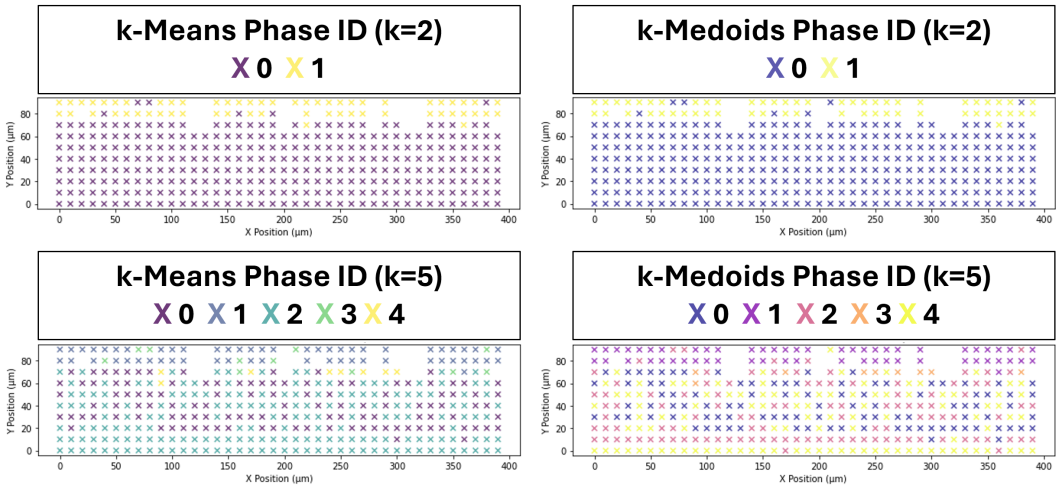

Figure 19. Spatial comparison of k-means and k-medoids classifications. At k = 2, both algorithms separate the high-hardness SiC region from the remaining joint constituents. At k = 5, both methods recover the principal spatial populations, although localized assignment differences appear within the mechanically overlapping braze region.

The sensitivity of the 20-mN results to the clustering method was evaluated by applying k-means and k-medoids to the same standardized feature set, ln(H), ln(E), and Z (Figure 20). The hardness (H) and stiffness (S) were chosen to compare cluster populations even though S was not used to drive clustering in this standard feature set. The two methods produced similar populations and only modest shifts between the corresponding cluster centers. After the cluster labels were matched by maximum membership overlap, 344 of 376 measurements retained the same assignment; the 32 reassigned measurements (8.5%) were concentrated primarily between the overlapping intermediate-hardness populations. The high-hardness SiC population and the small low-hardness artifact population were unchanged. Thus, the principal mechanical populations were largely insensitive to whether their centers were defined by arithmetic means or measured medoids, while the less distinct intermediate populations remained sensitive to the clustering method.

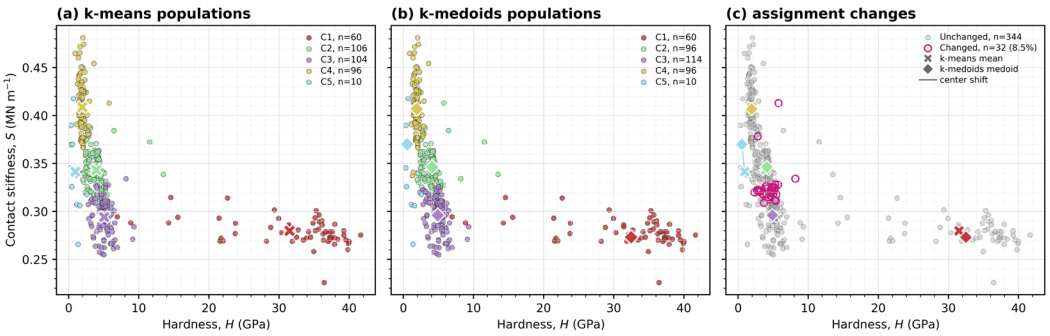

Figure 20. Comparison of k-means and k-medoids clustering for the 20-mN NanoBlitz array. Both algorithms were applied to the same five-cluster problem using standardized ln(*H*), ln(*E*), and surface position *Z* as input features; the resulting populations are projected onto hardness and contact stiffness for physical interpretation. (a) K-means populations, with arithmetic cluster means indicated by X symbols. (b) K-medoids populations, with medoids indicated by diamonds; each medoid corresponds to an experimentally measured indentation. (c) Comparison of the matched partitions, showing unchanged assignments in gray and reassigned measurements with magenta outlines.

The medoid representation offers several practical advantages for subsequent analysis. Unlike a k-means centroid, which is an arithmetic construction that may not correspond to any measured response, each medoid identifies an actual indentation. Its load-displacement curve, spatial position, surface condition, and neighboring microstructure can therefore be examined directly. This traceability provides a defensible route for selecting representative measurements for further microscopy, curve-level analysis, or targeted validation. Medoids are also less strongly influenced than means by extreme observations and asymmetric or heavy-tailed distributions, which may arise from porosity, phase-boundary interactions, surface artifacts, or fracture. These advantages do not establish that every medoid represents an intrinsic phase property, but they make the cluster center experimentally interpretable and auditable.

For this reason, the cluster centers reported here are descriptors of the mapped populations rather than independent measurements of intrinsic phase properties. Reference properties should instead be obtained from targeted measurements within sufficiently large regions of the constituent of interest.

3.10 Correspondence with the Microstructural Phase Map

Registration with the microstructural segmentation provides an independent test of the mechanically derived populations. Correspondence is strongest within the coarse regions. The SiC mechanical population coincides closely with the SiC region, and the Ti-6Al-4V population occupies the corresponding metallic side of the joint. This type of correlative comparison is particularly valuable in heterogeneous materials because it permits mechanical maps to be evaluated

against independently acquired microstructural information rather than assigning phase identity from mechanical properties alone.[12]

Correspondence decreases within the braze. This is expected from the characteristic dimensions of the reaction products. The Cu-Ti-rich boundary layer is only several micrometers thick, compared with an array pitch of approximately 10 μm, while the smaller Cu-Ti-rich dispersoids are submicrometer in dimension. These features are therefore unlikely to be sampled repeatedly by indents whose mechanically affected volumes remain entirely within a single constituent. Indentation size and spacing have both been shown to influence the ability of high-speed mapping to separate phases statistically.[8]

The microscopy and indentation measurements also resolve different physical quantities. Image segmentation is sensitive to optical contrast and morphology at length scales substantially smaller than the indentation spacing. Nanoindentation integrates mechanical response over a finite volume beneath the contact. A thin reaction product can therefore be readily visible by microscopy yet fail to generate a distinct indentation population. Conversely, a mechanically graded region may be evident in the indentation map without corresponding to a sharply bounded image class. Correlative mapping should therefore be treated as a comparison among complementary measurements, rather than a requirement that one map reproduce another exactly.[12]

This distinction changes the interpretation of the five-cluster analysis. The mechanical data reproduce the coarse architecture of the joint, including SiC, Ti-6Al-4V, and mechanically distinguishable regions within the braze. They do not reproduce all five microstructural classes individually. One population is dominated by pore-affected measurements, while two of the finest reaction products are poorly matched to the spatial resolution of the indentation experiment. The $k = 5$ solution is therefore useful as a test against the microstructural model, but it should not be presented as a five-phase mechanical map.

3.11 Implications of High-Density Indentation Mapping

Several practical conclusions can be drawn from these results for future experiments on heterogeneous interfaces.

First, indentation load and array spacing should be selected from the dimensions of the microstructural features that the experiment is intended to distinguish. Statistical sophistication cannot recover a constituent that is rarely or never sampled independently. Ideally, the smallest ROI should contain multiple indent centers while remaining sufficiently large relative to the indentation interaction volume to

minimize boundary contributions. The systematic effects of depth and spacing demonstrated by Besharatloo and Wheeler[8] support treating these variables as part of the experimental design rather than merely acquisition settings. For future studies, it may be beneficial to control indentation depth instead of indentation load to maintain a consistent sampling volume for each measurement.

Second, measurements on large, independently identifiable constituents provide essential anchors for interpreting dense arrays. The reference measurements on SiC and Ti-6Al-4V make it possible to recognize both the expected end-member responses and measurements that cannot reasonably represent either constituent. For an unknown multiphase material, targeted indentation of independently identified phases should therefore precede or accompany large-area mapping whenever possible.

Third, mechanical clusters should initially be interpreted as populations rather than phases. A cluster may represent a phase, a composition gradient, a boundary-affected response, porosity, or some combination of these. Phase identity should be assigned only after spatial registration with independent microstructural or compositional measurements. This is consistent with the broader development of correlative nanoindentation approaches.[12]

Fourth, k-medoids offers a useful default for heterogeneous experimental datasets when unusual measurements are expected. Its principal advantage here is not superior phase discovery. Rather, it reduces the influence of extreme observations on cluster representatives and, importantly, represents each population with an actual experiment that can be inspected afterward.[15,16] The close agreement with k-means for the strongly separated populations and divergence for the weakly separated populations further suggests that comparison between clustering methods can serve as a useful robustness check. A population that exists only under one reasonable clustering formulation deserves greater scrutiny.

Finally, spatial information should be used primarily for validation rather than to force mechanically coherent maps. Excluding X and Y from the present clustering allows the spatial banding of the mechanical populations to serve as independent evidence. Surface height Z is different because it is a measured response associated with local surface relief; however, its use requires care. Large-scale specimen tilt or curvature should be removed or shown to be negligible so that Z does not indirectly encode lateral position. The value of Z should therefore be established experimentally for each material system rather than assumed to be universally beneficial.

3.12 Limitations

The present work does not provide a one-to-one mechanical measurement of every reaction product in the interface. The principal limitation is spatial resolution: the smallest Cu-Ti-rich features approach or fall below the sampling and interaction scales of the indentation array. The 10- and 20-mN arrays also sampled adjacent microstructures, preventing the observed differences from being assigned uniquely to load.

The array measurements are additionally affected by indentation size effects, phase-boundary interactions, local porosity, and potentially phase-dependent pile-up (i.e., on ductile phases with high E/H) or surface relief.[8,21,23] These effects reinforce the distinction between cluster-center properties and intrinsic constituent properties. No resampling-based uncertainty analysis was performed on the cluster assignments, so individual labels should not be interpreted as having quantified classification confidence.

Finally, the optical segmentation provides a spatially dense reference rather than independent phase identification. Its phase interpretation derives from the accompanying microscopy and compositional characterization. Standardless XEDS measurements are similarly treated as compositional fingerprints rather than certified quantitative analyses. These limitations do not prevent identification of the coarse mechanical architecture of the joint, but they constrain claims concerning individual reaction products.

4. Conclusions

This study used spatially registered nanoindentation and microstructural characterization to determine how much of the mechanical architecture of an SiC/Ti-6Al-4V active-braze interface can be resolved experimentally. The principal conclusions are as follows:

1) The approximately 100-μm braze interlayer is mechanically heterogeneous. In addition to the SiC and Ti-6Al-4V end members, the indentation arrays identify at least two mechanically distinguishable populations within the braze. These populations are spatially organized across the interface even though lateral position was not supplied to the clustering algorithms.
2) Independent reference measurements are necessary for interpreting high-density arrays. Reference hardness and modulus were 30.94 ± 0.98 GPa and 495.74 ± 3.97 GPa for SiC, and 4.28 ± 0.10 GPa and 131.58 ± 1.20 GPa for Ti-6Al-4V. Array-derived cluster centers should not be substituted for these

values because indentation depth, indentation strain rate, boundary sampling, porosity, and surface conditions alter the apparent response.

3) Spatial resolution, rather than clustering method, is the primary limitation on phase identification. The micron-sized Cu-Ti-rich boundary layer and submicrometer dispersoids cannot be sampled reliably as independent mechanical populations with the present approximately 10-μm array pitch and indentation interaction volume. A more elaborate clustering algorithm cannot recover information that was not resolved experimentally.
4) K-medoids is useful for this type of experimental dataset because its representatives are actual indents and because unusual measurements have less influence on those representatives than they do on k-means centroids. Nevertheless, k-medoids and k-means agree closely when the mechanical populations are strongly separated and diverge primarily where the populations overlap. K-medoids should therefore be viewed as a robust and experimentally interpretable analysis tool, not as a substitute for adequate spatial resolution or independent phase characterization.
5) The pore-affected population illustrates an important benefit of retaining unusual measurements during exploratory analysis. Its very low stiffness and hardness, large penetration depth, and location within the porous SiC region distinguish it from the material-related populations. Such measurements can contain useful information about why an indentation response is anomalous even when they cannot be used to estimate phase properties.
6) For future high-density indentation studies of interfaces, the most important experimental choices are to characterize the relevant feature dimensions before selecting load and spacing, obtain independent reference measurements where possible, register mechanical measurements with microscopy or compositional maps, and treat mechanically derived clusters as populations until phase identity is independently supported. Under these conditions, clustering provides a useful means of revealing mechanical heterogeneity that may be obscured in conventional single-property distributions.

Taken together, these results suggest that the limiting step in mechanical phase mapping is often experimental resolution rather than the choice of a clustering algorithm. Future studies should therefore prioritize correlative microscopy, appropriate indentation volume, sufficient sampling density, and traceability of individual measurements before increasing the complexity of the statistical analysis.

5. References

1. Liu Y, Huang ZR, Liu XJ. Joining of sintered silicon carbide using ternary Ag-Cu-Ti active brazing alloy. Ceram Int. 2009;35:3479–3484. https://doi.org/10.1016/j.ceramint.2009.03.016

2. Moszner F et al. Mechanical behavior of SiC joints brazed using an active Ag-Cu-In-Ti braze at elevated temperatures. Int J Appl Ceram Technol. 2017;14:703–711. https://doi.org/10.1111/ijac.12689

3. Elrefaey A, Tillmann W. Effect of brazing parameters on microstructure and mechanical properties of titanium joints. J Mater Process Technol. 2009;209:4842–4849. https://doi.org/10.1016/j.jmatprotec.2009.01.006

4. Hernández-Rivera E, Hirsch SG, Butler B. Mesh generation from energy dispersive spectroscopy data of multiphase microstructures. DEVCOM Army Research Laboratory (US); 2025. Report No.: ARL-TN-1267.

5. Constantinides G, Chandran KSR, Ulm F-J, Van Vliet KJ. Grid indentation analysis of composite microstructure and mechanics: principles and validation. Mater Sci Eng A. 2006;430:189–202. https://doi.org/10.1016/j.msea.2006.05.125

6. Randall NX, Vandamme M, Ulm F-J. Nanoindentation analysis as a two-dimensional tool for mapping the mechanical properties of complex surfaces. J Mater Res. 2009;24:679–690. https://doi.org/10.1557/jmr.2009.0149

7. Rossi E, Wheeler JM, Sebastiani M. High-speed nanoindentation mapping: a review of recent advances and applications. Curr Opin Solid State Mater Sci. 2023;27:101107. https://doi.org/10.1016/j.cossms.2023.101107

8. Besharatloo H, Wheeler JM. Influence of indentation size and spacing on statistical phase analysis via high-speed nanoindentation mapping of metal alloys. J Mater Res. 2021;36:2198–2212. https://doi.org/10.1557/s43578-021-00214-5

9. Wheeler JM, Gan B, Spolenak R. Combinatorial investigation of the Ni-Ta system via correlated high-speed nanoindentation and EDX mapping. Small Methods. 2022;6:e2101084. https://doi.org/10.1002/smtd.202101084

10. Zhang C, Bos C, Sandfeld S, Schwaiger R. Unsupervised learning of nanoindentation data to infer microstructural details of complex materials. Front Mater. 2024;11:1440608. https://doi.org/10.3389/fmats.2024.1440608

11. Ortiz-Membrado L, Benitez R, Llanes L, Jiménez-Piqué E. High-speed nanoindentation data analysis of WC-based cemented carbides using Gaussian mixture model clustering and skew-normal mixture: beyond Gaussian deconvolution. Int J Refract Metals Hard Mater. 2025;126:106917. https://doi.org/10.1016/j.ijrmhm.2024.106917

12. Magazzeni CM et al. Nanoindentation in multi-modal map combinations: a correlative approach to local mechanical property assessment. J Mater Res. 2021;36:2235–2250. https://doi.org/10.1557/s43578-020-00035-y

13. Lloyd SP. Least squares quantization in PCM. IEEE Trans Inf Theory. 1982;28:129–137. https://doi.org/10.1109/TIT.1982.1056489

14. Jain AK. Data clustering: 50 years beyond K-means. Pattern Recognit Lett. 2010;31:651–666. https://doi.org/10.1016/j.patrec.2009.09.011

15. Schubert E, Rousseeuw PJ. Fast and eager k-medoids clustering: O(k) runtime improvement of the PAM, CLARA, and CLARANS algorithms. Inf Syst. 2021;101:101804. https://doi.org/10.1016/j.is.2021.101804

16. Chen X, Hou D, Han Y, Ding X, Hua P. Clustering analysis of grid nanoindentation data for cementitious materials. J Mater Sci. 2021;56:12238–12255. https://doi.org/10.1007/s10853-021-05848-8

17. Morgan Braze Alloys. InCuSil ABA technical datasheet [date unknown]. https://www.morganbrazealloys.com/media/vp5jchbd/incusil-aba.pdf

18. Ong FS et al. Residual stress induced failure of Ti-6Al-4V/Si3N4 joints brazed with Ag-Cu-Ti filler: the effects of brazing zone's elasto-plasticity and ceramics' intrinsic properties. J Eur Ceram Soc. 2021;41:6319–6329. https://doi.org/10.1016/j.jeurceramsoc.2021.06.038

19. Newbury DE, Ritchie NWM. Is scanning electron microscopy/energy dispersive X-ray spectrometry (SEM/EDS) quantitative? Scanning. 2013;35:141–168. https://doi.org/10.1002/sca.21041

20. Arganda-Carreras I et al. Trainable WEKA Segmentation: a machine learning tool for microscopy pixel classification. Bioinformatics. 2017;33:2424–2426. https://doi.org/10.1093/bioinformatics/btx180

21. Oliver WC, Pharr GM. An improved technique for determining hardness and elastic modulus using load and displacement sensing indentation experiments. J Mater Res. 1992;7:1564–1583. https://doi.org/10.1557/JMR.1992.1564

22. Ashby MF. The deformation of plastically non-homogeneous materials. Philos Mag. 1970;21:399–424. https://doi.org/10.1080/14786437008238426

23. Nix WD, Gao H. Indentation size effects in crystalline materials: a law for strain gradient plasticity. J Mech Phys Solids. 1998;46:411–425. https://doi.org/10.1016/S0022-5096(97)00086-0

24. Maier V et al. Nanoindentation strain-rate jump tests for determining the local strain-rate sensitivity in nanocrystalline Ni and ultrafine-grained Al. J Mater Res. 2011;26:1421–1430. https://doi.org/10.1557/jmr.2011.156

25. Oliver WC, Pharr GM. Measurement of hardness and elastic modulus by instrumented indentation: advances in understanding and refinements to methodology. J Mater Res. 2004;19:3–20. https://doi.org/10.1557/jmr.2004.19.1.3

26. Rossi E et al. A high-throughput framework for pile-up correction in high-speed nanoindentation maps. Mater Des. 2025;251:113708. https://doi.org/10.1016/j.matdes.2025.113708

27. Rousseeuw PJ. Silhouettes: a graphical aid to the interpretation and validation of cluster analysis. J Comput Appl Math. 1987;20:53–65. https://doi.org/10.1016/0377-0427(87)90125-7

28. Bolshakov A, Pharr GM. Influences of pileup on the measurement of mechanical properties by load and depth sensing indentation techniques. J Mater Res. 1998;13:1049–1058. https://doi.org/10.1557/JMR.1998.0146

29. Jun T-S, Armstrong DEJ, Britton TB. A nanoindentation investigation of local strain rate sensitivity in dual-phase Ti alloys. J Alloys Compd. 2016;672:282–291. https://doi.org/10.1016/j.jallcom.2016.02.146

30. Kaushik HC et al. Indentation strain rate sensitivity of laser-powder bed fused and electron beam melted Ti-6Al-4V. Vacuum. 2022;195:110690. https://doi.org/10.1016/j.vacuum.2021.110690

31. Tibshirani R, Walther G, Hastie T. Estimating the number of clusters in a data set via the gap statistic. J R Stat Soc Series B Stat Methodol. 2001;63:411–423. https://doi.org/10.1111/1467-9868.00293

List of Symbols, Abbreviations, and Acronyms

BSE	Backscattered Electron
CBS	Concentric Backscatter
CTE	Coefficient of Thermal Expansion
FCC	Face-Centered Cubic
ROI	Region of Interest
SEM	Scanning Electron Microscope
SiC	Silicon Carbide
SRS	Strain Rate Sensitivity
Ti64	Ti-6Al-4V Titanium Alloy
WEKA	Waikato Environment for Knowledge Analysis
XEDS	X-ray Energy Dispersive Spectroscopy
XPS	X-ray Photoelectron Spectroscopy
E	Reduced Elastic Modulus
H	Hardness
H_0	Nix–Gao Asymptotic (Size-Effect-Free) Hardness
h	Contact Depth
h^*	Nix–Gao Characteristic Length
k	Number of Clusters
m	Strain-Rate Sensitivity Exponent
r	Pearson Correlation Coefficient
S	Contact Stiffness
Z	Surface Height (Z Position)
σ	Standard Deviation

1 (PDF)	DEFENSE TECHNICAL INFORMATION CTR DTIC OCA
1 (PDF)	DEVCOM ARL FCDD RLB CB TECH LIB